Ablation of *Tmem65* Causes Lethal Mitochondrial Encephalomyopathy in Mouse

Yingfan Zhang[1], T. Bradley Willingham[1], Laura Reyes[2], Chengyu Liu[3], Danielle Springer[4], Audrey Noguchi[4], Angel M. Aponte[5], Jeeva Munasinghe[6], Raul Covian[7], Brian Glancy[1,8,9]

1. Muscle Energetics Laboratory, NHLBI
2. Quantitative Medical Imaging, NIBIB
3. Transgenic Core, NHLBI
4. Murine Phenotyping Core, NHLBI
5. Proteomics Core, NHLBI
6. In Vivo NMR Center, NINDS
7. Laboratory of Cardiac Energetics, NHLBI
8. NIAMS
9. Corresponding author, Brian Glancy. Building 10, B1D412, 10 Center Drive, NHLBI, NIH, Bethesda, MD 20892, USA. Phone: 1-301-496-2679; Email: glancybp@nhlbi.nih.gov

The authors have declared that no conflict of interest exists.

ABSTRACT:

Depletion of transmembrane protein 65 (TMEM65) in a patient with a homozygous point mutation in the *TMEM65* gene splice site was reported to result in mitochondrial dysfunction and severe encephalomyopathy(1), indicating the clinical importance of TMEM65. However, the function of TMEM65 remains unknown, and the specific subcellular localization of TMEM65 to either the mitochondrial inner membrane or cardiac intercalated disc remains controversial. Here, we generated a *Tmem65* reporter mouse as well as whole-body and tissue-specific *Tmem65* knockout (KO) mice to investigate the localization and function of TMEM65. We show that TMEM65 is localized to mitochondria in heart, skeletal muscle, and throughout the brain. Both whole-body and nervous system-specific *Tmem65* KO resulted in severe growth retardation and sudden death following seizures ~3 weeks after birth indicating TMEM65 is indispensable for normal brain function. Cardiac-specific *Tmem65* KO mice were viable and fertile but had reduced mitochondrial content and cardiac stress response. Skeletal muscle-specific *Tmem65* KO led to progressive, adult-onset myopathy manifested by wasting of muscle fibers, upregulation of one-carbon metabolic pathways, and reduced whole-body metabolic efficiency. These results highlight the effectiveness of a *Tmem65* KO mouse model to recapitulate and further interrogate the clinical phenotypes associated with a loss of TMEM65.

INTRODUCTION:

There are more than 1,500 proteins within the mitochondrion, yet the functions of most of these proteins are not fully understood (2, 3). Mitochondria contain their own genome, the mitochondrial DNA, which only encodes 13 proteins as subunits of the oxidative phosphorylation enzyme complexes. Therefore, mitochondria highly rely on nuclear DNA for protein production. Most of the mitochondrial proteins are encoded by nuclear DNA, synthesized in the cytoplasm, and imported and resorted to the mitochondria (4, 5). Mitochondrial proteins are critical to maintain a variety of cellular functions such as energy conversion and homeostasis, calcium signaling, apoptosis-programmed cell death, etc. (2, 3, 6). Mutations or loss of mitochondrial proteins can lead to a spectrum of mitochondrial disorders affecting multiple systems and organs including neurodegenerative disorders, cardiomyopathies, skeletal myopathies, metabolic syndrome, and malfunctions of other organs and systems (2).

Transmembrane protein 65 (TMEM65) was first reported in MitoCarta, an inventory of more than 1000 mammalian mitochondrial proteins (7), and initially considered to be localized to the inner mitochondrial membrane with three putative transmembrane domains, an N-terminus facing to the mitochondrial matrix, and a C-terminus in the mitochondrial intermembrane space (8). TMEM65 is encoded by nuclear DNA, and contains a mitochondrial targeting sequence at the N-terminus of the protein so that it can be imported into mitochondria (8). The expression of TMEM65 is regulated by the Steroid Receptor RNA Activator (SRA), which is a long non-coding RNA functioning by forming a ribonucleoprotein complex with leucine-rich pentatricopeptide repeat-containing protein (LRPPRC) and the Stem–Loop-Interacting RNA-binding Protein (SLIRP) (9). Despite the abundance of information available surrounding the structure and regulation of this protein, the function of TMEM65 is unclear. Interestingly, TMEM65 has also been suggested to be a plasma membrane protein localized to the intercalated discs in cardiac myocytes where it functions as a novel regulator that interacts with connexin 43 (CX43) to modulate gap junction communication (10). However, a critical role for TMEM65 in cardiac function was not supported

by a recent report of a patient with severe mitochondrial encephalomyopathy caused by a significant loss in TMEM65 expression, as the patient did not show any evidence of cardiomyopathy (1).

In this study, we generated a *Tmem65* reporter mouse to resolve whether TMEM65 is localized to mitochondria and/or intercalated discs. Additionally, we generated a conditional *Tmem65* KO mouse model to systematically ablate TMEM65 in different tissues and investigate the functional role of *Tmem65*. We found that systemic KO of *Tmem65* in mice leads to sudden death at wean age accompanied with growth retardation, epilepsy, and neurodegenerative pathological changes in the brain. Conditional KO of *Tmem65* in different tissues confirmed that ablation of TMEM65 in the nervous system is lethal, while ablation of TMEM65 in heart and skeletal muscle also leads to deteriorating mitochondrial symptoms. In addition, we found that ablation of TMEM65 in primary fibroblasts affected mitochondrial structure and function with lower mitochondrial membrane potential and NADH redox status, increased NADH flux, more fragmented mitochondrial networks, and increased mitophagy. The phenotypic similarity between our *Tmem65* KO mouse model and the recently reported patient with *TMEM65* mutation highlights the clinical relevance of this mouse model for advancing our understanding of the function of this indispensable protein.

RESULTS:

Generation of a *Tmem65* reporter mouse confirms TMEM65 as a mitochondrial protein

To resolve whether TMEM65 is localized to mitochondria (1, 8), intercalated discs (10), or both, we first examined the expression of TMEM65 in mice using several commercially available anti-TMEM65 antibodies. However, we found that the available antibodies showed high levels of non-specificity in Western blotting analyses (Suppl. Fig. 1). Therefore, a *Tmem65-V5* in frame knock-in mouse model was generated by inserting a V5 tag to the C-terminus of the *Tmem65* gene before the stop codon so that endogenous TMEM65 protein with a V5 tag is expressed in this mouse model (Suppl. Fig. 2A). The V5

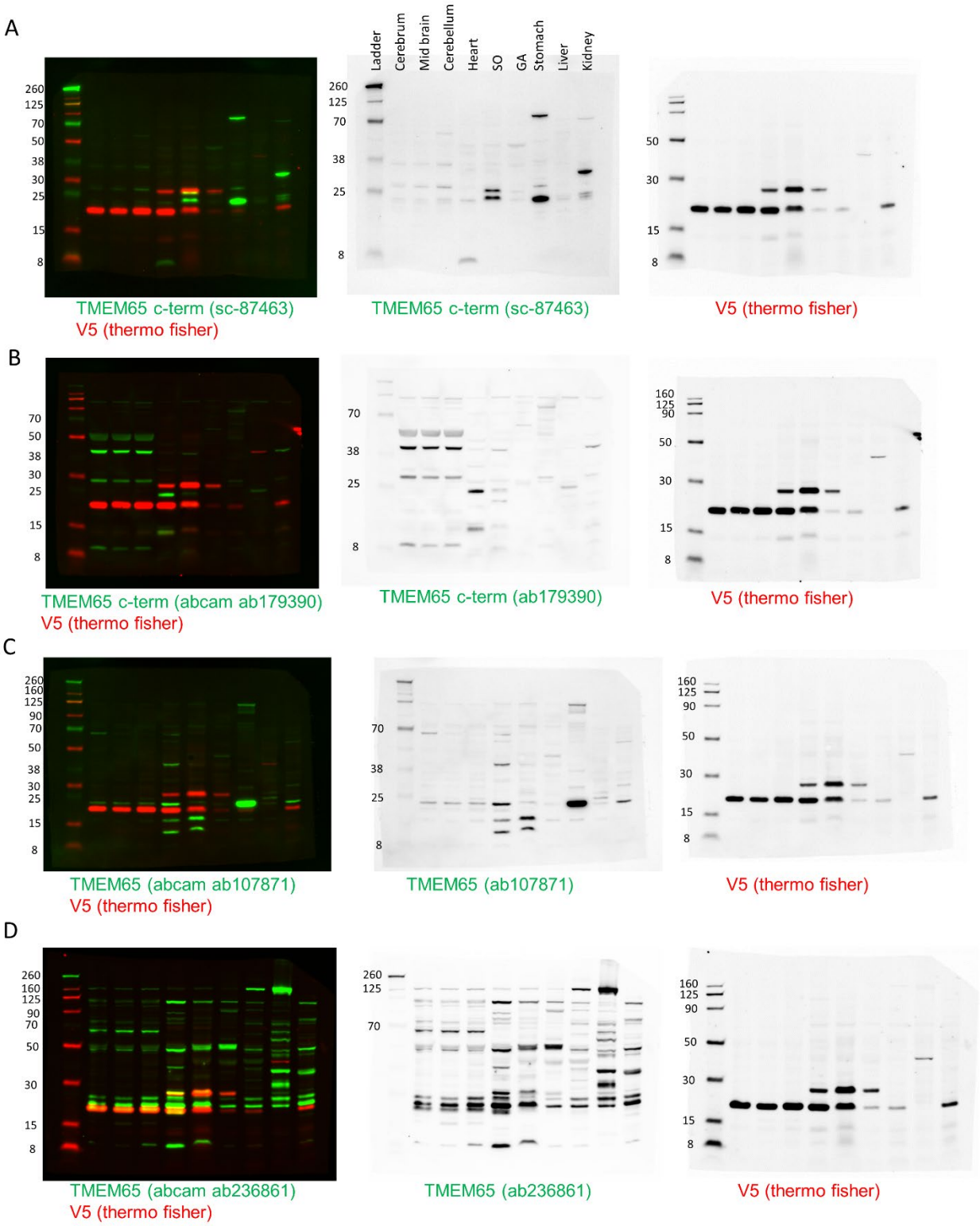

Supplemental figure 1. Western blot analysis of tissue lysates from TMEM65-V5 mouse to test specificity of anti-TMEM65 antibodies. (A) Anti-TMEM65 antibody from Santa Cruz (sc-87463). (B) Anti-TMEM65 antibody from Abcam (ab179390). (C) Anti-TMEM65 antibody from Abcam (ab107871). (D) Anti-TMEM65 antibody from Abcam (ab236861).

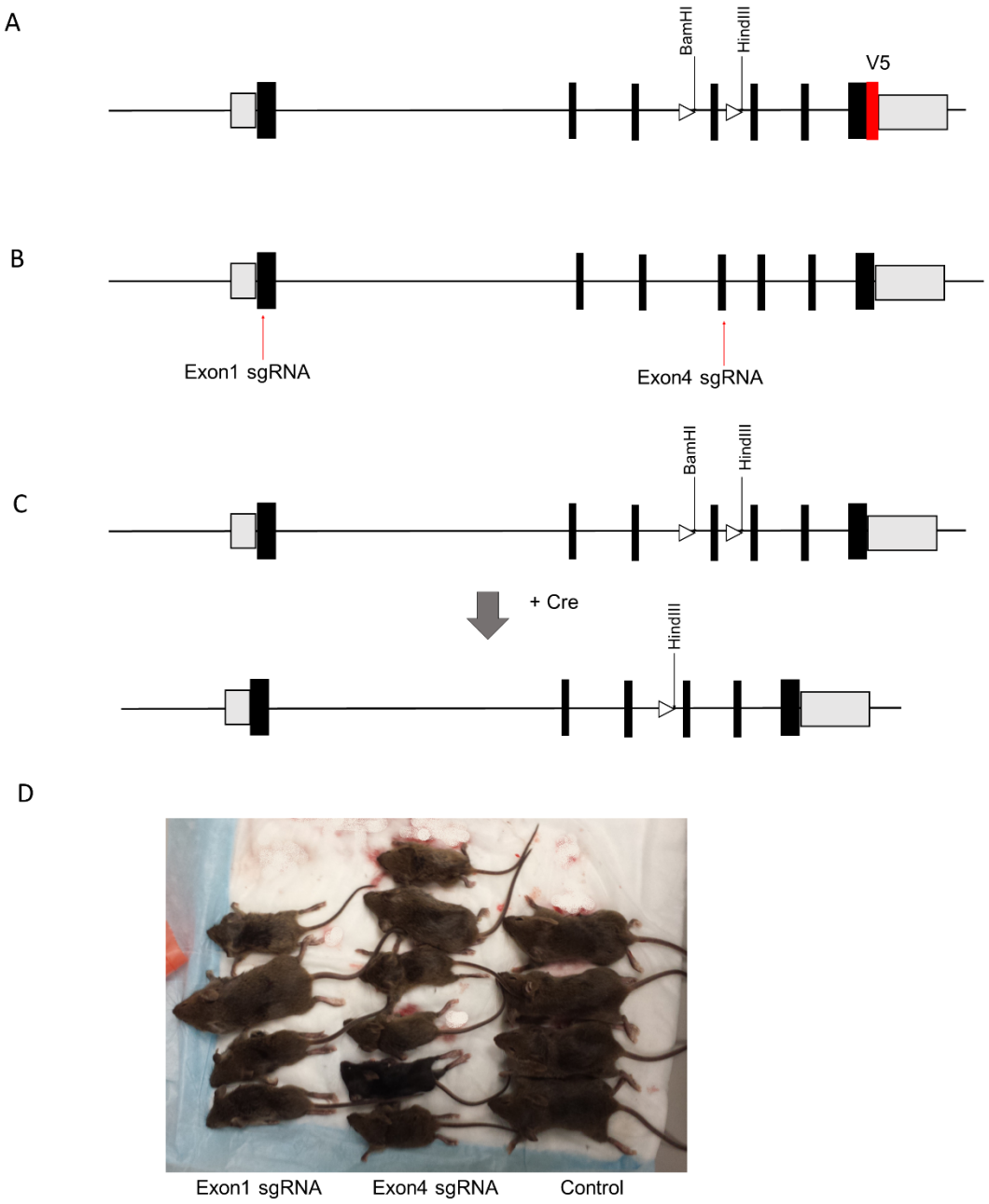

Supplemental figure 2. Design of the *Tmem65* mouse models. (A) V5 sequence was knocked in to exon7 immediately before the stop codon to make a V5 in frame KI mouse model. (B) Design of CRISPR KO mouse model. SgRNA was designed to target either exon1 or exon4 for KO of *Tmem65*. (C) Floxed *Tmem65* mouse model was generated by knockin of two loxP sequences in front of and after exon4 of *Tmem65* gene, respectively. Two restriction site sequences, BamHI and HindIII, were also introduced with loxP sequences as indicated in the figure. When Cre recombinase is expressed, the sequence between the two loxP sites will be removed. Solid black box: translated region of exon; solid grey box: untranslated region of exon; solid red box: V5 sequence; triangle: loxP sequence. (D) Three groups of mice were generated with sgRNA targeted to exon1, exon4, or a negative control without sgRNA. Picture shows mice of *Tmem65* KO by sgRNA to exon1 or exon4 were smaller than the control at P21.

tag is a short, 1.4 KDa peptide containing 14 amino acids (11) that is not likely to compromise the structure, function, or localization of the TMEM65 protein, and highly specific antibodies to V5 are widely available to study the expression of TMEM65-V5 protein. Tissue lysates from homozygous TMEM65-V5 mice (*Tmem65*$^{+V5/+V5}$) were subject to Western blotting analysis with anti-V5 antibody, and TMEM65-V5 was present in a variety of tissues including brain, heart, fast and slow skeletal muscles, smooth muscle, and kidney (Fig. 1A). Unlike the most commonly used anti-TMEM65 antibody (Sigma-Aldrich) which showed two to five bands in each tissue, only two bands were detected with the anti-V5 antibody, indicating two isoforms of TMEM65-V5 existing in some tissues. The molecular weights of the two TMEM65-V5 bands are consistent with the full length TMEM65-V5 protein (26 KDa) and a truncated TMEM65-V5 protein (20 KDa) losing part of its sequence at the N-terminus where the mitochondrial targeting sequence is located (8).

To determine the localization of TMEM65's expression in brain, heart and skeletal muscle tissues, immunofluorescence experiments of these mouse tissues were conducted. In brain tissues from homozygous *Tmem65*$^{+V5/+V5}$ mouse, V5 was shown to colocalize with mitochondrial ATP synthase subunit A (ATP5A) in neurons at different brain regions, indicating TMEM65 is a mitochondrial protein in brain tissues (Fig. 1B, Suppl Fig. 3A). In isolated cardiac myocytes from wild type mice (*Tmem65*$^{+/+}$) using anti-TMEM65 antibody (Sigma-Aldrich), TMEM65 was shown to colocalize with mitochondrial complex IV, but not with N-cadherin, an intercalated disc protein marker, indicating TMEM65 is also a mitochondrial protein in the mouse heart (Suppl Fig. 3C and 3D). Immunofluorescence of *Tmem65*$^{+V5/+V5}$ heart sections showed that TMEM65-V5 protein did not colocalize with Connexin 43, an intercalated disc marker, but was present in a typical mitochondrial pattern (Suppl Fig. 3B upper row). Indeed, TMEM65-V5 colocalized with TOM20, a mitochondrial outer membrane marker (Fig. 1C); and finally, when *Tmem65*$^{+V5/+V5}$ heart sections were stained with both anti-V5 antibody and anti-TMEM65 antibody (Sigma-Aldrich), both antibodies stained a typical mitochondrial pattern and colocalized. However, the anti-TMEM65 antibody also stained some of the nuclei and intercalated discs, indicating that the

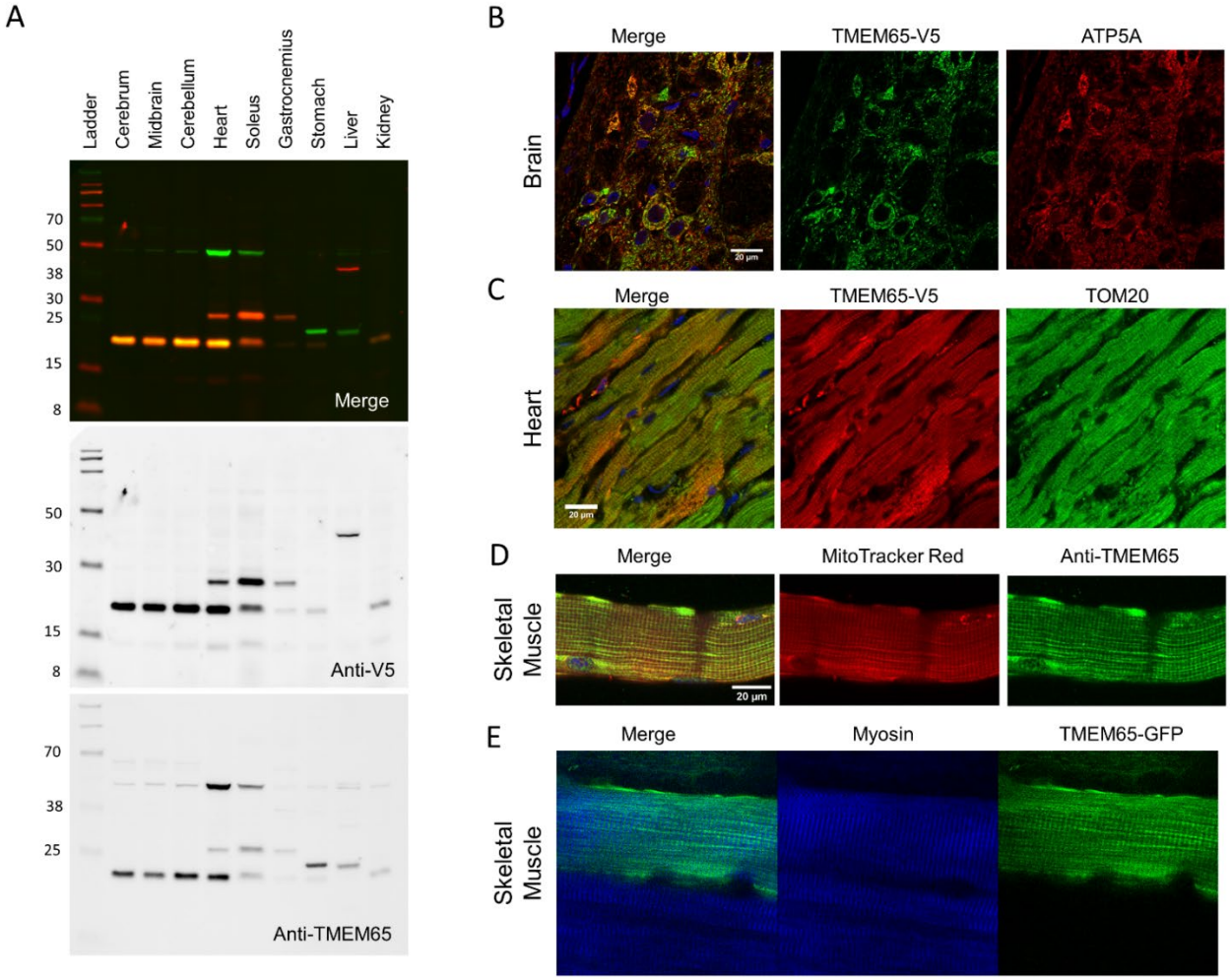

Figure 1. TMEM65 is a mitochondrial protein expressed in different mouse tissues including brain, heart and skeletal muscles. (A) Representative Western blot analysis of different tissues from an adult *Tmem65-V5* mouse. Anti-V5 antibody and anti-TMEM65 antibody were used on the same blot to confirm TMEM65 expression in different tissues. (B) Brain section from adult *Tmem65-V5* mouse were stained with anti-V5 antibody and anti-ATP5A antibody to show colocalization of these two proteins and demonstrate that TMEM65 is a mitochondrial protein in the brain. (C) Heart frozen sections from TMEM65-V5 mouse were stained with anti-V5 and anti-TOM20 antibodies to show TMEM65 is a mitochondrial protein in mouse heart. (D) Isolated skeletal muscle fiber were stained MitoTracker Red and anti-TMEM65 antibody to show TMEM65 is a mitochondrial protein in skeletal muscle fiber. (E) Mouse TA muscle was transfected with TMEM65-GFP plasmid with electroporation in vivo, and the muscle was imaged with 2-photon microscope in vivo. The GFP signal in the transfected muscle fiber showed a typical mitochondrial network in skeletal muscle. Blue channel shows secondary-harmonic generation of myosin in the muscle fiber.

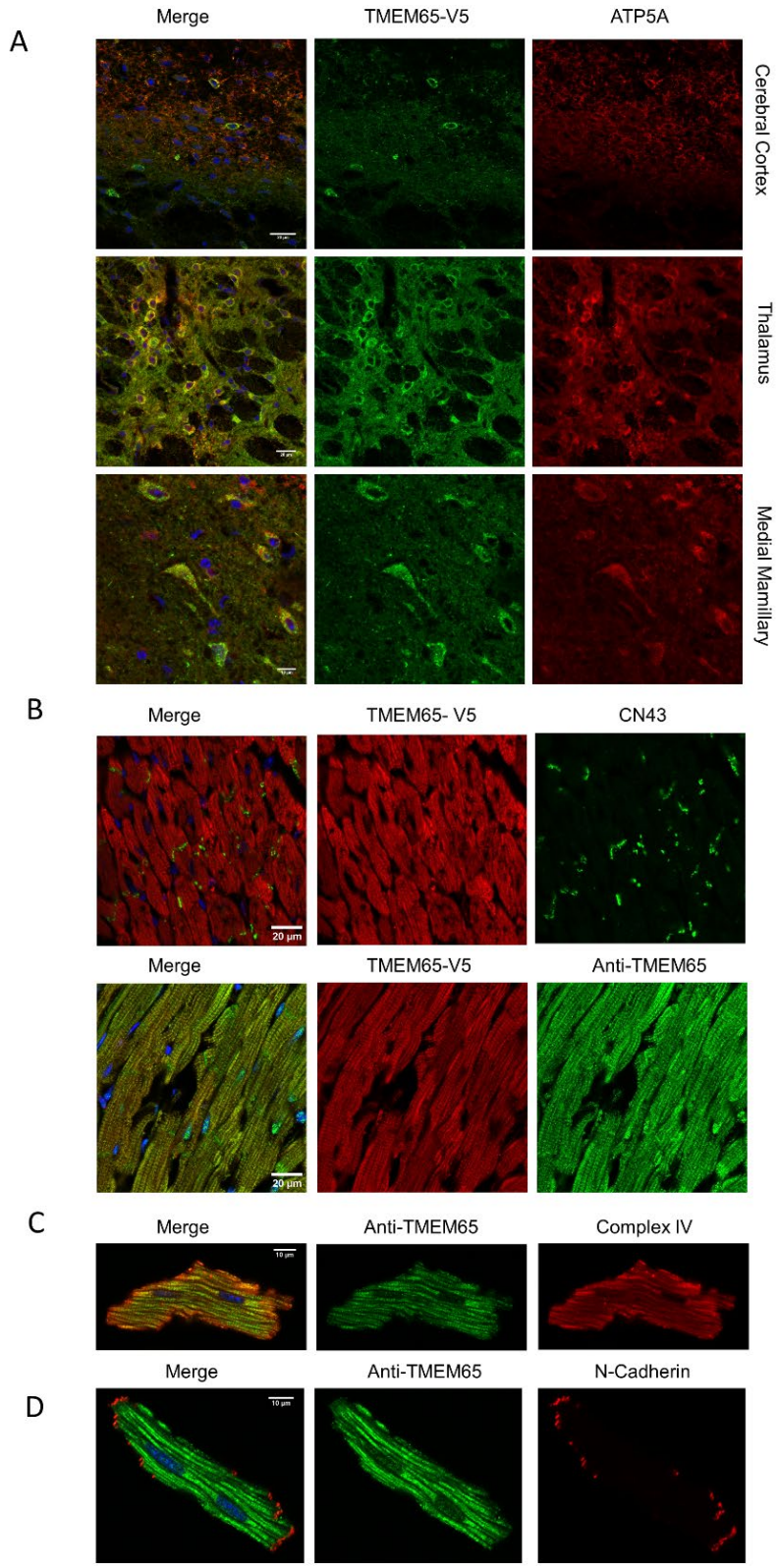

Supplemental figure 3. TMEM65 is a mitochondrial protein expressed in different mouse tissues including brain, heart and skeletal muscles. (A) Brain sections from different parts of adult *Tmem65-V5* mouse were stained with anti-V5 antibody and anti-ATP5A antibody to show colocalization of these two proteins and demonstrate that TMEM65 is a mitochondrial protein in the brain. (B) Upper row: Heart frozen sections from *Tmem65-V5* mouse were stained with anti-V5 and anti-Connexin43 antibodies to show TMEM65 is not an intercalated disc protein in mouse heart. Lower row: Heart frozen section from *Tmem65-V5* mouse was stained with anti-V5 and anti-TMEM65 (Sigma-Aldrich) antibodies. (C) Isolated cardiac myocyte were stained with anti-TMEM65 antibody and anti-complex IV antibody. (D) Isolated cardiac myocyte were stained with anti-TMEM65 antibody and anti-N-Cadherin antibody to show that TMEM65 is not colocalized with N-Cadherin, an intercalated disc marker in the heart.

immunofluorescent staining in these two structures in heart tissue was due to non-specificity (Suppl Fig. 3B, lower row). In isolated skeletal muscle fibers, anti-TMEM65 antibody was shown to colocalize with a mitochondrial membrane potential sensitive fluorescent dye, MitoTracker Red (Fig. 1D). Additionally, *Tmem65-Gfp* plasmid was electroporated into Tibialis anterior (TA) muscle of wild type *Tmem65*$^{+/+}$ mouse, and the TA muscle was imaged *in vivo* using 2-photon microscopy. The resultant TMEM65-GFP signal showed the characteristic grid-like mitochondrial network surrounding the contractile machinery in transfected muscle fibers (Fig. 1E), further indicating TMEM65 is also a mitochondrial protein in skeletal muscle.

Systemic loss of TMEM65 in mice results in death by seizures at three weeks of age

To investigate the impact of TMEM65 in mice, two different knockout (KO) approaches were used. First, to directly knock out *Tmem65* systemically, the *Tmem65* gene was disrupted by sgRNAs targeting exon1, exon4, or both using standard CRISPR technologies (Suppl. Fig. 2B). In a second method, a conditional KO of *Tmem65* mouse line was generated by inserting loxP sites to flank exon4 of the gene (Suppl. Fig. 2C). The floxed *Tmem65* line (denoted *Tmem65*$^{flox/flox}$) was then crossed with a CMV-cre mouse line to achieve whole body KO (12) of *Tmem65*. *Tmem65* KO mice (*Tmem65*$^{-/-}$) from both methods showed the same phenotype. *Tmem65*$^{-/-}$ mice experienced growth retardation compared to their littermates (Fig. 2A and 2B, Suppl. Fig. 2D); their body weights were significantly lower than their littermate controls at every timepoint (postnatal day (P) 5, P10, P15 and P20) (Fig. 2B). After P15, *Tmem65*$^{-/-}$ mice failed to continue gaining bodyweight and their bodyweights decreased, indicating growth regression after P15 (Fig. 2B). All *Tmem65*$^{-/-}$ mice died between P11 and P30 with average life span of 21.7±3.6 days (Fig. 2C). Epilepsy episodes were recorded with home cage monitoring and were often observed immediately prior to their sudden death (Supplemental Video 1). Weakness, occasional pulling/paralysis of hindlimb, and uncoordinated walking appeared with increasing age, culminating in death. In addition, the *Tmem65*$^{-/-}$

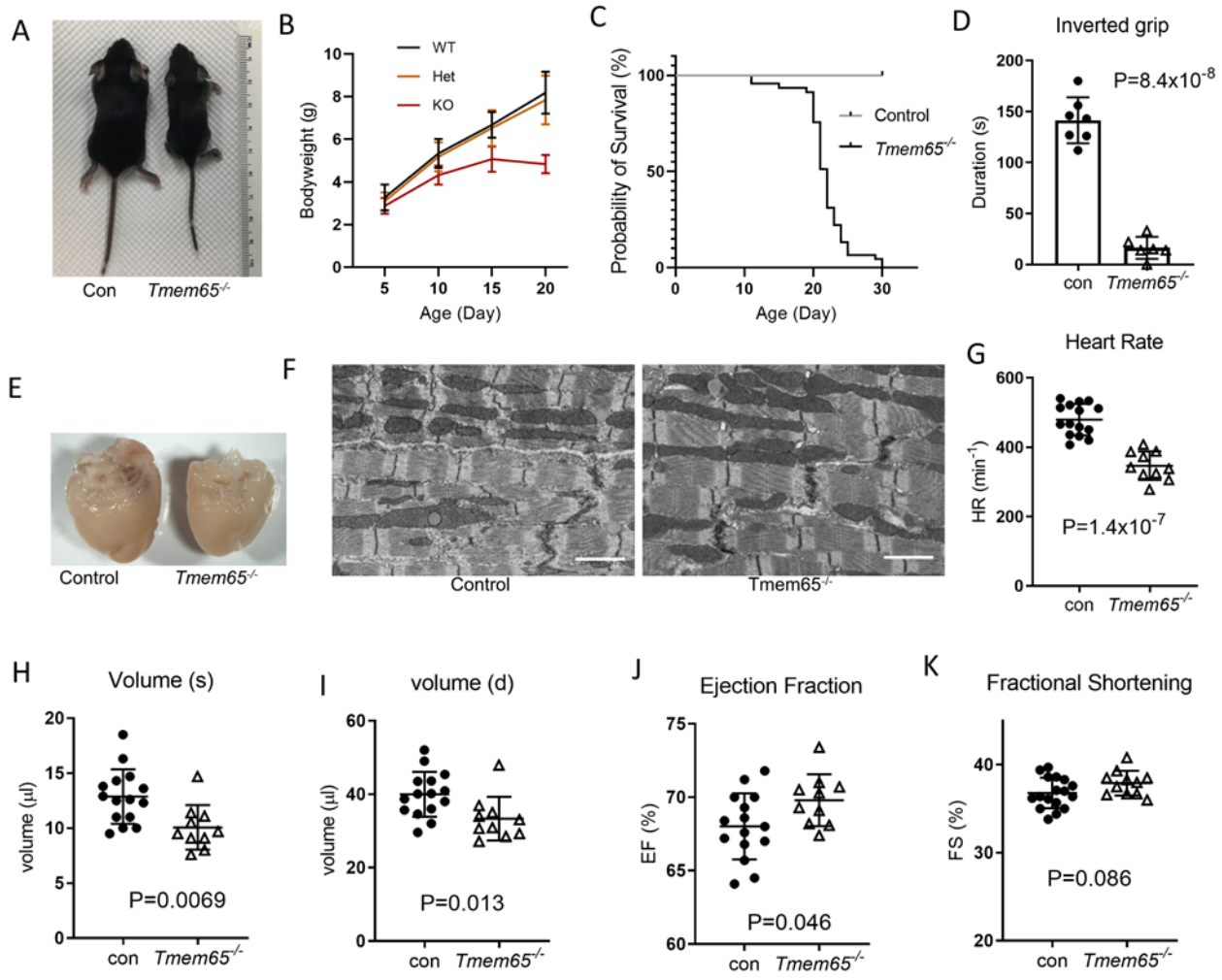

Figure 2. Loss of TMEM65 in mice results in early death around weaning age coupled with epilepsy and skeletal and cardiac muscle manifestation. (A) Control *Tmem65*$^{+/+}$ and *Tmem65*$^{-/-}$ littermate pups at P20. (B) Body weights of littermates measured at P5, P10, P15 and P20. Compared to littermate controls (WT *Tmem65*$^{+/+}$, heterozygous *Tmem65*$^{+/-}$), *Tmem65*$^{-/-}$ pups were significantly smaller at all checkpoints, indicating growth retardation. (C) Control *Tmem65*$^{+/+}$ and *Tmem65*$^{-/-}$ pups survival chart shows that *Tmem65*$^{-/-}$ pups died between P11 and P30, with an average life span of 21.71±3.57 days. (D) Inverted grip test was done on weaning day of P21. *Tmem65*$^{-/-}$ pups had a significant shorter duration, indicating weakness of muscles in these pups. (E) Hearts from P21 littermates of control *Tmem65*$^{+/+}$ and *Tmem65*$^{-/-}$ pups. (F) EM images of P20 hearts of littermates. Muscle contractile apparatus, mitochondria and intercalated discs are all normal in *Tmem65*$^{-/-}$ heart. Bar, 1 µm. (G) *Tmem65*$^{-/-}$ mouse had a lower heart rate compared to littermates *Tmem65*$^{+/+}$ at P21. (H-K) Echocardiology results from P21 control *Tmem65*$^{+/+}$ and *Tmem65*$^{-/-}$ littermates. Systolic volumes (H) and diastolic volumes (I) were significantly lower, while ejection fraction (J) was higher in P21 *Tmem65*$^{-/-}$ hearts. Percentage of fractional shortening (K) was similar between control and *Tmem65*$^{-/-}$ littermates.

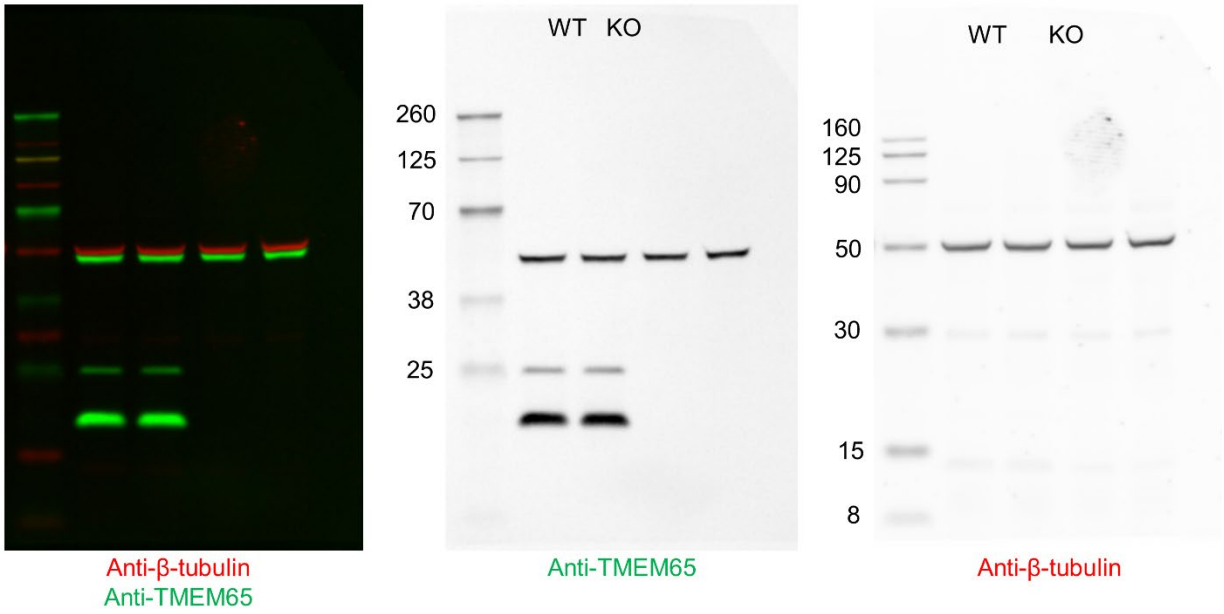

Supplemental figure 4. Western blot analysis of heart tissues from WT control and *Tmem65*$^{-/-}$ mice at P20. Anti-TMEM65 antibody from Sigma-Aldrich (HPA025020) were used to detect TMEM65 protein in the blot. In *Tmem65*$^{-/-}$ heart tissue, 25KD and 19KD bands were lost, while ~50KD band still existed, indicating ~50KD band is a nonspecific band for this antibody.

mice were generally weaker than littermate controls and were not able to maintain their grip during an inverted grid test at P21 (Fig. 2D).

Due to the high mitochondrial TMEM65 expression in the heart, we examined cardiac structure and function in control and *Tmem65*$^{-/-}$ mice. The complete loss of TMEM65 in the hearts of whole body *Tmem65* KO mice was confirmed at P20 by Western blotting of heart tissue lysates (Suppl Fig. 4). At P20, hearts from *Tmem65*$^{-/-}$ mice are smaller compared to those of WT littermates (Fig. 2E), which is consistent with the smaller body weights of *Tmem65*$^{-/-}$ mice (Fig. 2B). Imaging cardiomyocytes by electron microscopy did not reveal any clear ultrastructural abnormalities within the mitochondria, sarcomeres, or intercalated discs in *Tmem65*$^{-/-}$ hearts as all appeared similar to wild type littermate controls (Fig. 2F). However, *Tmem65*$^{-/-}$ mice at P21 had a significantly lower heart rate than controls (Fig. 2G). Since the heart rate of mice and other small mammals has been reported to increase during postnatal development (13), the lower heart rates in *Tmem65*$^{-/-}$ mice may be related to the delayed development and smaller body size of the *Tmem65*$^{-/-}$ mice. Echocardiography revealed that both systolic heart volume and diastolic heart volume are smaller in *Tmem65*$^{-/-}$ hearts (Fig. 2H and 2I), consistent with the finding that *Tmem65*$^{-/-}$ hearts are smaller than control hearts. The ejection fraction of *Tmem65*$^{-/-}$ mice was slightly higher than control littermates, while the percentage of fractional shortening was similar between controls and *Tmem65*$^{-/-}$ mice, indicating a normal to mildly increased contractility in *Tmem65*$^{-/-}$ mice (Fig. 2J and 2K). The mildly increased ejection fraction in *Tmem65*$^{-/-}$ heart could be the result of lower heart rate of the *Tmem65*$^{-/-}$ heart, which will provide more time to allow the *Tmem65*$^{-/-}$ heart to relax before next contraction, or could indicate a compensatory process to the lower heart rates in *Tmem65*$^{-/-}$ mice. Arrhythmias were not observed in P21 *Tmem65*$^{-/-}$ mice.

Cardiomyocyte-specific loss of TMEM65 leads to lower mitochondrial content and a reduced stress response but not death

To further study the role of TMEM65 in cardiac function, a heart-specific *Tmem65* KO mouse line was established by crossing the *Tmem65*$^{flox/flox}$ mice with Nkx2-5 Cre mice (14). *Tmem65* heart-specific KO mice (denoted *Tmem65*$^{flox/flox}$ *::Nkx2-5*^{Cre}) are viable and fertile and exhibit no obvious phenotypic abnormalities. Western blot analysis with heart tissue lysates from *Tmem65*$^{flox/flox}$ *::Nkx2-5*^{Cre} mice showed the total loss of the 19KDa and 25KDa bands of truncated and full length TMEM65 protein, confirming that TMEM65 was completely knocked out in hearts from *Tmem65*$^{flox/flox}$ *::Nkx2-5*^{Cre} mice (Fig. 3A), similar to in the whole body *Tmem65*$^{-/-}$ mice (Fig. 3A). Notably, these results further highlight the non-specificity of the higher molecular weight bands when using anti-TMEM65 antibody (Sigma-Aldrich). To further confirm the localization of TMEM65 in the heart, sections from adult control and *Tmem65*$^{flox/flox}$ *::Nkx2-5*^{Cre} mouse hearts were stained with anti-TMEM65 antibody for immunofluorescence. In *Tmem65*$^{flox/flox}$ control heart sections, anti-TMEM65 antibody mostly stained mitochondria, but also partially stained some intercalated discs and some nuclei in control heart sections (Fig. 3B, left). In TMEM65 KO heart sections from *Tmem65*$^{flox/flox}$ *::Nkx2-5*^{Cre} mice with the same anti-TMEM65 antibody, TMEM65 mitochondrial staining was totally lost, while intercalated disc staining and nuclei staining still existed, confirming TMEM65 is a mitochondrial protein in the heart (Fig. 3B right). The presence of intercalated discs and nuclei staining in the TMEM65 KO heart again indicates nonspecific staining of the anti-TMEM65 antibody in the heart, similar to the Western blot analyses (Fig. 3A, upper bands of ~48KDa). Phosphotungstic acid-haematoxylin (PTAH) staining of heart sections from 8 month old *Tmem65*$^{flox/flox}$ control and *Tmem65*$^{flox/flox}$ *::Nkx2-5*^{Cre} mice revealed normal striation patterns and intercalated discs in the *Tmem65*$^{flox/flox}$ *::Nkx2-5*^{Cre} hearts (Fig. 4A) consistent with the lack of ultrastructural alterations in the heart of whole body KO mice (Fig. 2F).

To test the role of TMEM65 in the response to cardiac stress, one year old mice were subjected to a Dobutamine challenge during echocardiography. In one year old mice, baseline ejection fraction and heart rate were similar between *Tmem65*$^{flox/flox}$ controls and *Tmem65*$^{flox/flox}$ *::Nkx2-5*^{Cre} mice (Fig. 4B and 4C),

indicating baseline heart function was not affected by the KO of *Tmem65* in the heart. Additionally, no

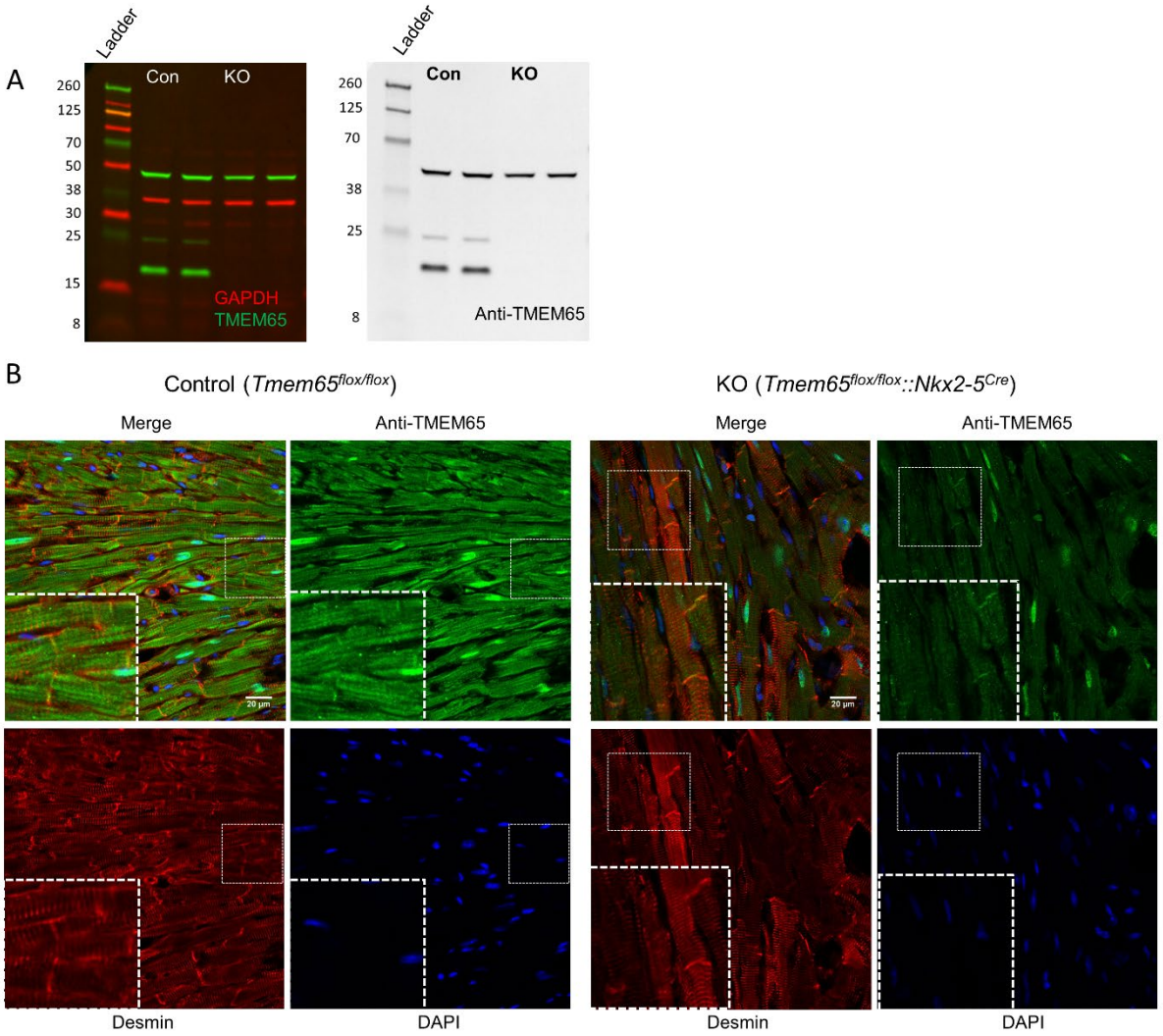

Figure 3. Confirming loss of TMEM65 in the heart of *Tmem65$^{flox/flox}$::Nkx2-5^{Cre}* mice. (A) Western blot analysis of adult control and *Tmem65$^{flox/flox}$::Nkx2-5^{Cre}* hearts shows complete KO of TMEM65 protein, while the non-specific band of ~50 KDa still exists in the TMEM65 KO heart. (B) Immunofluorescence of adult mouse heart sections with anti-TMEM65 antibody and anti-Desmin antibody. Control section shows anti-TMEM65 antibody mainly stained mitochondria. The immunostaining of anti-TMEM65 antibody to intercalated discs and some of the nuclei were non-specific since these staining still exists in TMEM65 KO heart.

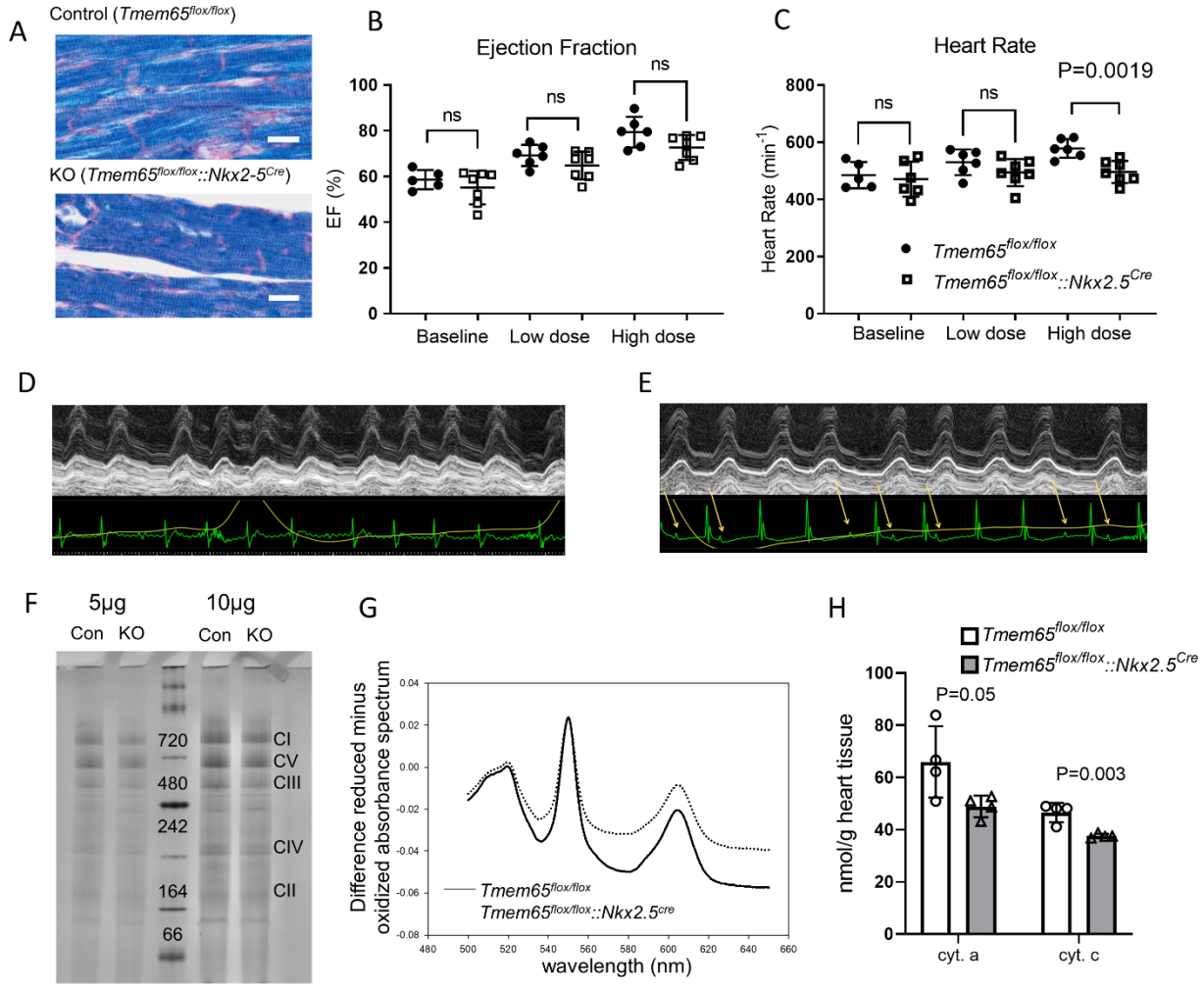

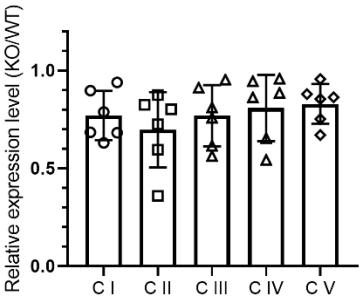

Figure 4. Cardiomyocyte-specific loss of TMEM65 leads to lower mitochondrial content and a reduced stress response but not death. (A) PTAH stain of 8 months old control and *Tmem65*$^{flox/flox}$*::Nkx2-5*^{Cre} hearts shows normal heart structure, including intercalated discs and mitochondrial striation in TMEM65 KO heart compared to control heart. Bar: 20 µm. (B-E) Dobutamine challenge during ECG test of one year old mice. (B) Ejection fraction showed no significant changes between control and *Tmem65*$^{flox/flox}$*::Nkx2-5*^{Cre} hearts in baseline and during Dobutamine challenge. (C) Heart rates were comparable between control and *Tmem65*$^{flox/flox}$*::Nkx2-5*^{Cre} hearts during baseline and low dose Dobutamine challenge. During high dose challenge, heart rates of *Tmem65*$^{flox/flox}$*::Nkx2-5*^{Cre} hearts were significantly lower than controls. (D-E) Arrhythmia was found in a few *Tmem65*$^{flox/flox}$*::Nkx2-5*^{Cre} mice during high dose Dobutamine challenge, including abnormal heart rhythm showing prolonged beat or possibly dropped beat every four beats (D), and cardiac arrythmia with increasing PR intervals, and occasional QRS complexes not proceeded with a p wave (E). (F) Blue native PAGE gel of control and *Tmem65*$^{flox/flox}$*::Nkx2-5*^{Cre} heart lysates shows that expression levels of mitochondrial complexes in crude mitochondrial extract from TMEM65 KO heart are lower than control. Ladder with molecular weight is in the middle lane. Relative expression levels of mitochondrial complexes of *Tmem65*$^{flox/flox}$*::Nkx2-5*^{Cre} heart were compared to control. (G) Difference absorbance spectrum of cytochrome c (cyt. c) and cytochrome a (cyt. a) levels of heart tissues in a pair of 5-month-old *Tmem65*$^{flox/flox}$ and *Tmem65*$^{flox/flox}$*::Nkx2.5*^{Cre} littermates. (H) Spectrophotometric measurements of cyt. a and cyt. c amounts in heart tissue lysate from 5-month-old control *Tmem65*$^{flox/flox}$ and *Tmem65*$^{flox/flox}$*::Nkx2.5*^{Cre} mice (mean ± SD, n = 4).

arrhythmias were observed in *Tmem65*$^{flox/flox}$ *::Nkx2-5*^{Cre} mice during ECG examinations at baseline. While the high dose of dobutamine resulted in a significantly increased ejection fraction above baseline in both *Tmem65*$^{flox/flox}$ *::Nkx2-5*^{Cre} mice and controls, no ejection fraction differences were found between heart-specific *Tmem65* KO mice and their littermate controls (Fig. 4B). However, *Tmem65*$^{flox/flox}$ *::Nkx2-5*^{Cre} mice were unable to significantly increase their heart rate in response to the high dose Dobutamine challenge resulting in lower heart rates compared to littermate controls (Fig. 4C). Arrhythmias were also observed in some of the *Tmem65*$^{flox/flox}$ *::Nkx2-5*^{Cre} hearts during the high dose Dobutamine challenge (Fig. 4, D and E). These data suggest that mice lacking TMEM65 in their heart are unable to properly respond to periods of cardiac stress.

Since TMEM65 is localized to mitochondria, we next analyzed the composition of the respiratory chain complexes of the *Tmem65*$^{flox/flox}$ *::Nkx2-5*^{Cre} hearts. Crude mitochondrial extracts were harvested from heart tissue and subjected to Blue native PAGE for mitochondrial respiratory chain complexes quantification. Compared to littermate controls (*Tmem65*$^{flox/flox}$), *Tmem65*$^{flox/flox}$ *::Nkx2-5*^{Cre} hearts have systematically lower levels of all five respiratory chain complexes (Fig. 4F), ranged from 69.8% to 83.0% compared to the control levels. Spectral analysis of the heart tissue lysates (15) showed that cytochrome a level was about 25.8% lower, while cytochrome c level was about 19.3% lower in *Tmem65*$^{flox/flox}$ *::Nkx2-5*^{Cre} hearts compared to *Tmem65*$^{flox/flox}$ controls(Fig. 4G and 4H). These results suggest that cardiac-specific loss of TMEM65 leads to reduced mitochondrial respiratory chain content in the heart consistent with the reduced stress response manifested during the high dose Dobutamine challenge.

Loss of TMEM65 in brain causes neuronal vacuolar degeneration and sudden death

Western blot and immunofluorescence analysis showed that not only is TMEM65 highly expressed in mouse brain tissue, it is also a mitochondrial protein in the neurons in different parts of the brain (Fig. 1A and 1B, Suppl Fig. 3A). The epilepsy observed before sudden death of *Tmem65*$^{-/-}$ pups indicates defects in brain function of these mice. To find out if there are any structural abnormalities in the brain, MRI scanning of 20-23 days old littermates of control *Tmem65*$^{+/+}$ and *Tmem65*$^{-/-}$ brains was performed after

Magnevist pre-perfusion to enhance the contrast of brain tissue. We found that the volumes of *Tmem65*$^{-/-}$ brains were significantly smaller than those of the *Tmem65*$^{+/+}$ littermate controls measured with MRI (Fig. 5A and 5B), indicating a microcephaly phenotype. Volume decrease was most apparent in the regions of cerebral cortex and midbrain of the KO brains. Among the seven *Tmem65*$^{-/-}$ brains examined, diffusive lesions in the midbrain and brain stem regions were found in a 23 days old *Tmem65*$^{-/-}$ brain (Fig. 5A, right). This *Tmem65*$^{-/-}$ brain was also ~16.0% smaller compared to the *Tmem65*$^{+/+}$ littermate control, with thinner cortex and enlarged ventricles, indicating atrophy and loss of neurons in these areas, which are specific pathological changes in neurodegeneration(16). The *Tmem65*$^{-/-}$ cerebrum was also deformed as it was wider and shorter in axial plane, making it more round than control. Loss of TMEM65 in the brain was confirmed with Western blot analysis by the loss of the 20KDa bands in *Tmem65*$^{-/-}$ brains (Fig. 5C). Comparing H&E stained brain sections from P20-P22 *Tmem65*$^{-/-}$ and *Tmem65*$^{+/+}$ control mice, neuronal vacuolar degeneration was observed in many of the *Tmem65*$^{-/-}$ brain tissues as a remarkable pathological change (Fig. 5D). In brain sagittal sections, vacuolar neurons were found mainly in cerebral cortex, especially cingulate cortex above corpus callosum in cerebrum accompanied with nuclear shrinkage and condensation (Fig. 5D). In some of the *Tmem65*$^{-/-}$ brains, vacuolar neurons were also found in the brain stem in addition to the vacuolar neuron lesion in cerebral cortex area of the same brain (Suppl Fig.5 A and B), indicating that the vacuolar encephalopathy is quite diffusive in *Tmem65*$^{-/-}$ brain. Interestingly, vacuolation is a typical neurodegeneration found in Leigh syndrome and it could be the cause of epilepsy and sudden death in *Tmem65*$^{-/-}$ mice (17).

To confirm whether loss of TMEM65 in the brain causes the sudden death observed in whole body *Tmem65* KO mice, *Tmem65* was specifically knocked out in the mouse nervous system by crossing the floxed *Tmem65* mouse (*Tmem65*$^{flox/flox}$) with the Nestin-Cre mouse line, in which Cre recombinase expression was controlled by *Nestin* promoter and enhancer (18). Nestin-Cre driven TMEM65 ablation should start at an early stage of embryonic day 12.5 in the central and peripheral nervous system when Cre recombinase starts to express (19). Mice of nervous system specific KO of *Tmem65* (denoted

Tmem65$^{flox/flox}$*::Nes*^{Cre}) recapitulated sudden death in *Tmem65*$^{-/-}$ mice and died between P18-P29 with

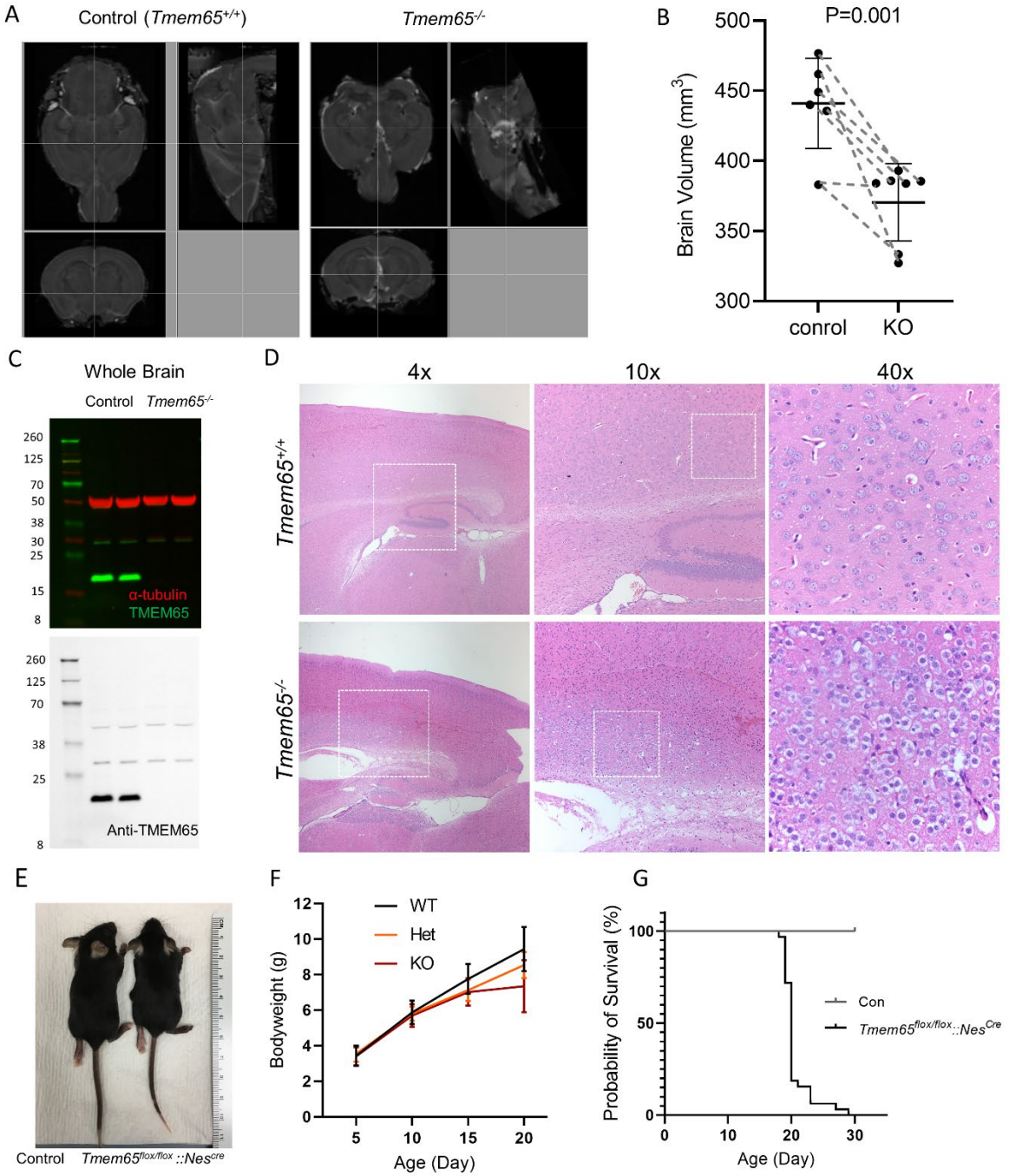

Figure 5. Loss of TMEM65 in brain causes neuronal vacuolar degeneration and sudden death. (A) MRI scan of a pair brains from P23 littermates show lesion and deformation of the *Tmem65*$^{-/-}$ brain. (B) Mouse brain volumes measured with MRI scan. Dash line indicates littermate pairs. (C) Western blot analysis of P20 brain tissues shows ablation of TMEM65 in *Tmem65*$^{-/-}$ brain. (D) H&E staining of brain sagittal sections show diffusive neuronal vacuolar degeneration in the cingulate cortex region. (E) Control and *Tmem65*$^{flox/flox}$ *::Nes*^{Cre} littermates at P20. (F) Body weights of littermates measured at P5, P10, P15 and P20. (G) Survival chart of controls and *Tmem65*$^{flox/flox}$ *::Nes*^{Cre} pups.

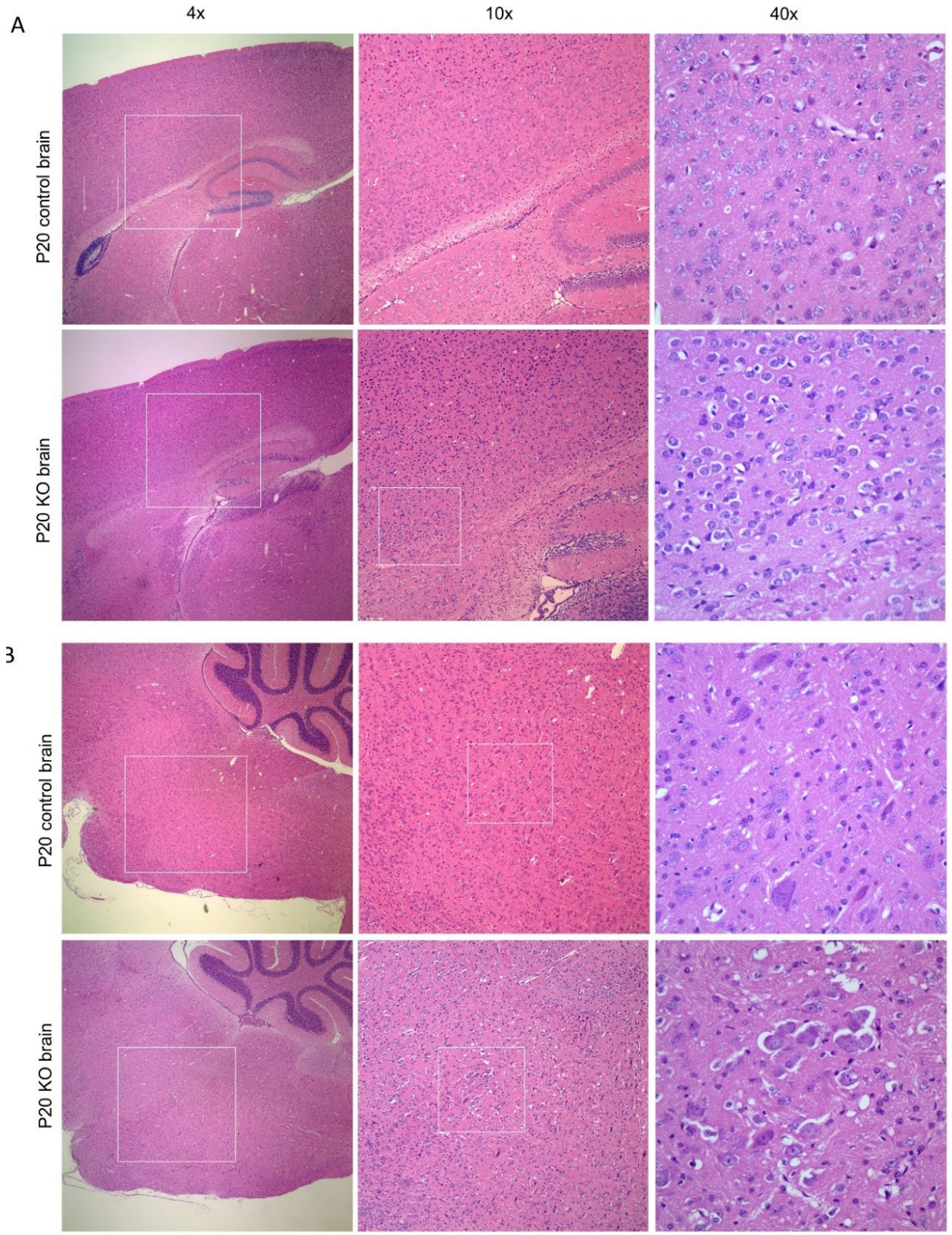

Supplemental figure 5. Brain lesion in a P20 *Tmem65*$^{-/-}$ mouse. H&E staining of brain sagittal sections show diffusive neuronal vacuolar degeneration in the cingulate cortex region (A), and brain stem area (B). Images were taken at 4x, 10x, and 40x.

average life span of 20.5±2.3 days (Fig. 5G). Although not as remarkable as the *Tmem65*$^{-/-}$ mice, *Tmem65*$^{flox/flox}$*::Nes*^{Cre} also developed growth retardation at P15 and P20 (Fig. 5E and 5F). Epilepsy episodes were also observed before sudden death with home cage monitoring. The phenotypic similarity between the whole-body KO *Tmem65*$^{-/-}$ mice and nervous system specific KO *Tmem65*$^{flox/flox}$*::Nes*^{Cre} mice confirmed that TMEM65 is extremely important for normal brain structure and function.

Loss of TMEM65 in skeletal muscle affects skeletal muscle metabolism and leads to muscular atrophy and body weight loss

Skeletal muscle contains a network of mitochondria which regulates the metabolism of the muscle with remarkable plasticity (20). TMEM65 was shown to be expressed in both fast-twitch and slow-twitch muscles, but the expression level detected by Western blot analysis was much higher in slow-twitch muscle, which contains a much more extensive of mitochondrial network compared to fast-twitch muscles (Fig. 1A). Immunofluorescent staining of TMEM65 in isolated muscle fiber and *in vivo* transfection of mouse TMEM65-GFP to skeletal muscle all confirmed that TMEM65 is a mitochondrial protein (Fig. 1D and 1E). To investigate if loss of TMEM65 in skeletal muscle mitochondria would affect skeletal muscle function, a mouse model of *Tmem65* specific KO in skeletal muscle tissue (denoted *Tmem65*$^{flox/flox}$*::Myf6*^{Cre}) was generated by crossing *Tmem65*$^{flox/flox}$ with *Myf6-Cre* line (21). In the *Myf6-Cre* line, *Cre* expression is specific to skeletal muscle and begins during later stages of embryonic development (22, 23).

Tmem65$^{flox/flox}$*::Myf6*^{Cre} mice are viable and fertile. However, the muscle specific KO mice stopped growing at 3 months old, and loss of bodyweight was observed afterwards (Fig. 6A) suggesting that TMEM65 is critical for maintenance of muscle mass. Both male and female showed the same trends, and the loss of muscle mass was remarkable at 6 months old. As shown in Fig. 6B, gastrocnemius muscle of *Tmem65*$^{flox/flox}$*::Myf6*^{Cre} mouse is much smaller compared to the same muscle from littermate controls. EchoMRI body composition analysis also confirmed that both fat mass and lean mass were lost in muscle specific KO mice at 6 months old (Fig. 6C). To monitor metabolic changes related to ablation of

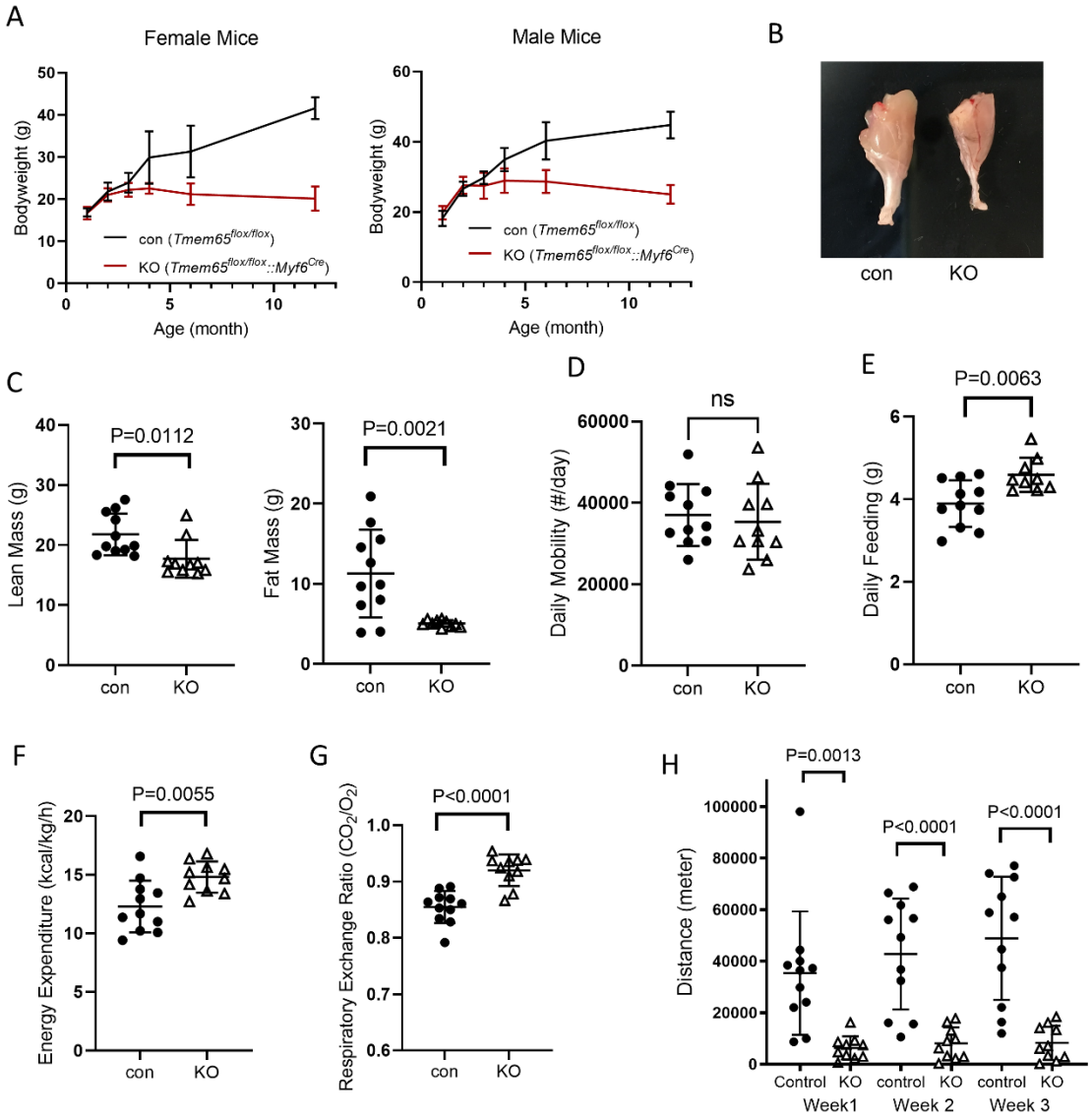

Figure 6. Loss of TMEM65 in skeletal muscle affects metabolism and leads to muscular atrophy and body weight loss. (A) Bodyweights of male and female mice at different ages. (B) Gastrocnemius muscles from 6-month-old control *Tmem65*$^{flox/flox}$ and *Tmem65*$^{flox/flox}$ *::Myf6*^{Cre} littermates. (C) EchoMRI body composition analysis of 6-month-old control *Tmem65*$^{flox/flox}$ and *Tmem65*$^{flox/flox}$ *::Myf6*^{Cre} littermates. (D-G) Metabolic parameters results from 6-month-old control *Tmem65*$^{flox/flox}$ and *Tmem65*$^{flox/flox}$ *::Myf6*^{Cre} littermates collected in metabolic cages (CLAMS) for simultaneous measurement. (H) Wheel running tests of 6-month-old control *Tmem65*$^{flox/flox}$ and *Tmem65*$^{flox/flox}$ *::Myf6*^{Cre} littermates collected in individual housing for 3 weeks.

TMEM65 in skeletal muscle, control and *Tmem65*$^{flox/flox}$*::Myf6*^{Cre} mice of 6 months of age were housed in metabolic cages called comprehensive lab animal monitoring system (CLAMS) for simultaneous measurement of metabolic parameters. *Tmem65*$^{flox/flox}$*::Myf6*^{Cre} mice had similar daily mobility compared to control mice (Fig. 6D). However, daily feeding, energy expenditure and respiratory exchange ratio

were all higher in *Tmem65*$^{flox/flox}$*::Myf6*^{Cre} mice compared to controls (Fig. 6, E-G), indicating a reduced metabolic efficiency in skeletal muscles of *Tmem65*$^{flox/flox}$*::Myf6*^{Cre} mice. To assess physical performance and endurance, 6-month-old mice were housed singly and subject to voluntary wheel running for 3 weeks. *Tmem65*$^{flox/flox}$*::Myf6*^{Cre} mice showed significantly lower running distance throughout the experiments (Fig. 6H), indicating loss of TMEM65 in skeletal muscle negatively affected running performance and endurance.

We next compared the soleus muscle from control and *Tmem65*$^{flox/flox}$*::Myf6*^{Cre} mice at 2 months old, 6 months old and 10 months old, and found that the cross section areas (CSA) of the muscle fibers from *Tmem65*$^{flox/flox}$*::Myf6*^{Cre} mice are smaller at these three time points (Fig. 7A and 7B). Muscle fiber-type assessment by immunofluorescent staining of antibodies to myosin heavy chain isoforms revealed that loss of TMEM65 led to a significant increase in type I fibers and reduction of type IIa fibers in *Tmem65*$^{flox/flox}$*::Myf6*^{Cre} soleus compared with control mice at 6 months old and 10 months old (Fig. 7A and 7C). The progressive loss of type IIa fibers in *Tmem65*$^{flox/flox}$*::Myf6*^{Cre} mice is consistent with the high expression of TMEM65 in type IIa muscle fibers compared to other fiber types (24).

To identify proteins and their underlying functions and pathways affected by ablation of TMEM65 in skeletal muscle, protein expression profiles of control and *Tmem65*$^{flox/flox}$*::Myf6*^{Cre} soleus muscle tissues at 2 months old and 10 months old were obtained using a tandem mass tag (TMT)-based proteomics approach. A total of 5425 proteins were identified for each group (Suppl. Dataset 1). At 2 months old, when significant phenotypic changes were not observed, 120 proteins had shown differentially expressed in protein abundance (P value <0.05) between controls and *Tmem65*$^{flox/flox}$*::Myf6*^{Cre} muscles (Fig. 8A and 8B, left). At 10 months old, when *Tmem65* KO in skeletal muscle showed a strong myopathy phenotype, 1541 proteins had changed significantly in abundance in *Tmem65*$^{flox/flox}$*::Myf6*^{Cre} muscles which correlated to the severity of the pathological changes in skeletal muscles (Fig. 8A and 8B, right). At 2 months old,

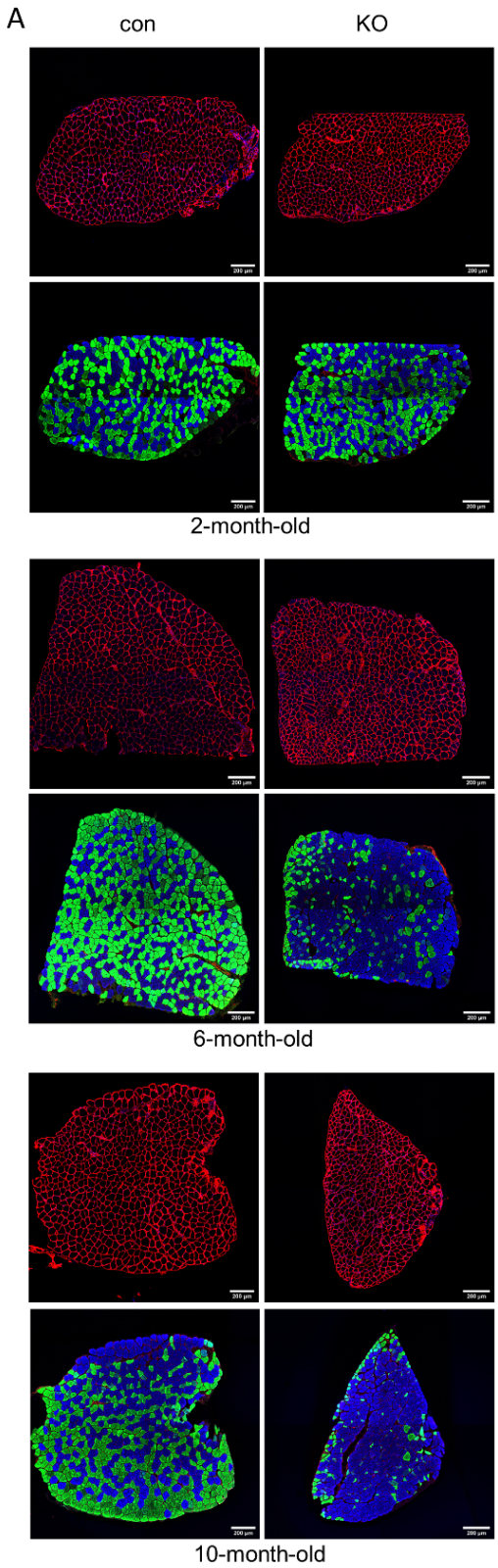

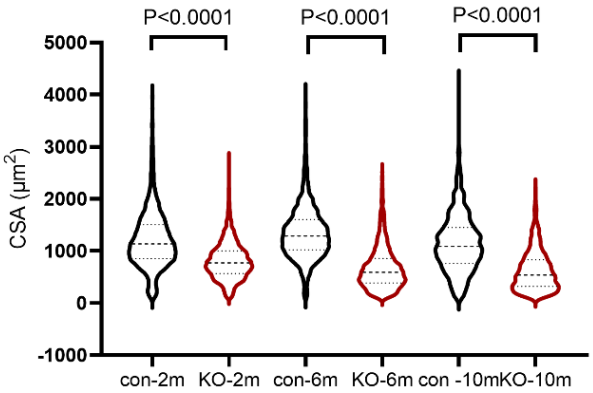

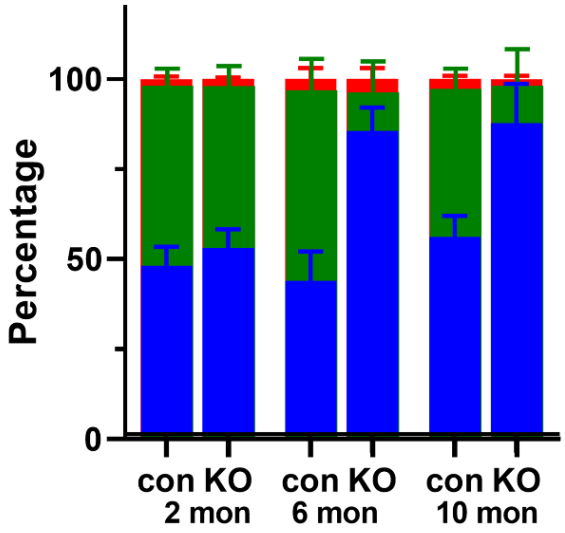

Figure 7. Loss of TMEM65 in skeletal muscle affects metabolism and leads to muscular atrophy and body weight loss (A). Immunofluorescence of soleus muscles from control *Tmem65*$^{flox/flox}$ and *Tmem65*$^{flox/flox}$ *::Myf6*^{Cre} littermates at 2 months old, 6 months old, and 10 months old. Anti-Laminin antibody staining (red, upper rows) delineated individual muscle fibers for cross-section area quantification and evaluation. Myosin isoforms were identified with specific antibodies to muscle type I (blue), IIa (green) and IIb (red), in lower rows. (B) Quantification of soleus muscle fiber cross section area from control *Tmem65*$^{flox/flox}$ and *Tmem65*$^{flox/flox}$ *::Myf6*^{Cre} littermates of different ages. (C) Quantification of myosin isoform composition in control *Tmem65*$^{flox/flox}$ and *Tmem65*$^{flox/flox}$ *::Myf6*^{Cre} soleus muscle cross sections at different age.

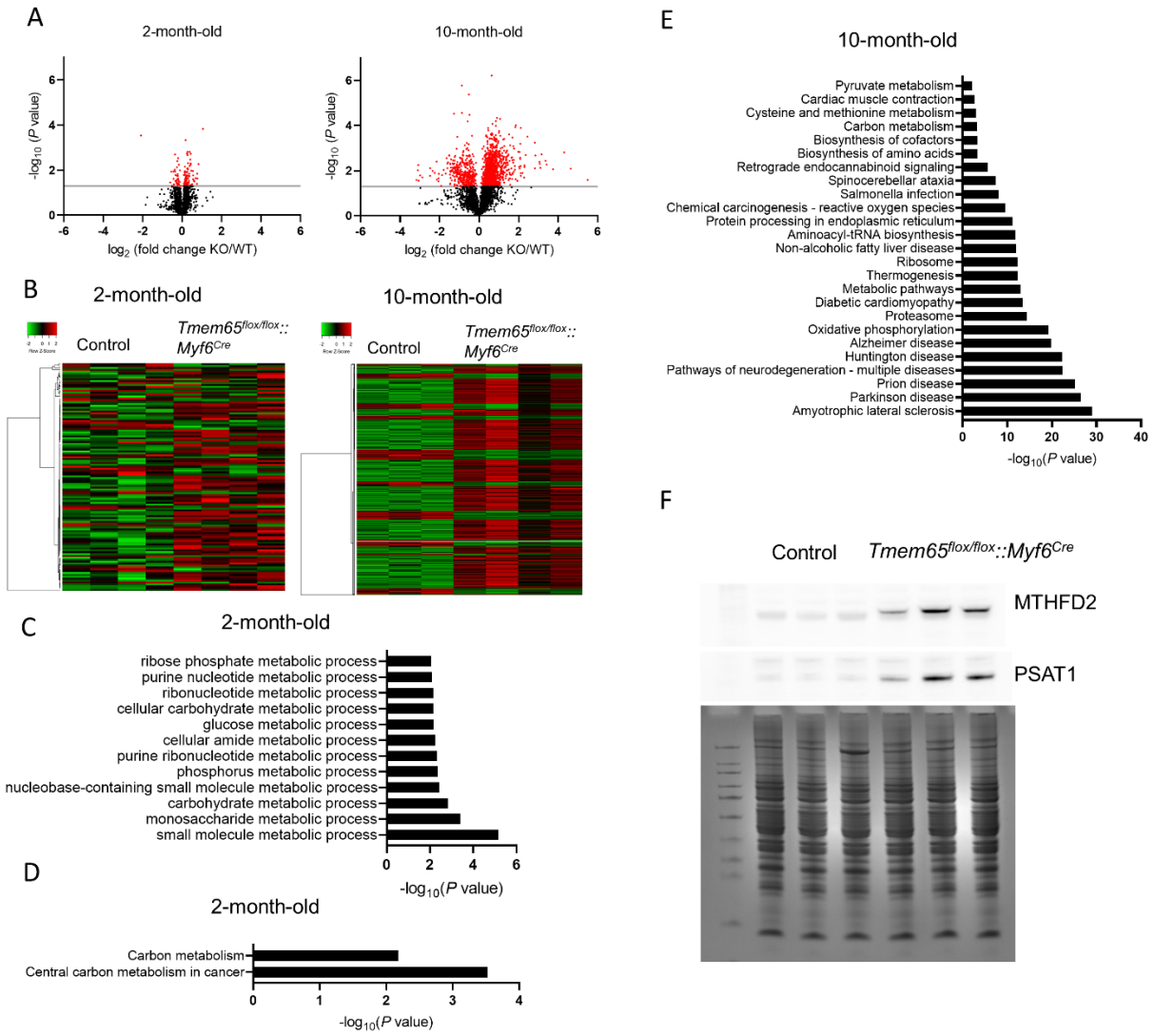

Figure 8. Skeletal muscle function and pathway changes caused by loss of Tmem65 in skeletal muscle. (A) Volcano plots of differentially abundant proteins of control *Tmem65*$^{flox/flox}$ and *Tmem65*$^{flox/flox}$ *::Myf6*^{Cre} soleus at 2 months old and 10 months old, respectively. Fold change represents KO/WT. (B) Heat maps of differentially abundant proteins from control control *Tmem65*$^{flox/flox}$ and *Tmem65*$^{flox/flox}$ *::Myf6*^{Cre} soleus at 2 months old and 10 months old, respectively. (C) Biological processes affected in *Tmem65*$^{flox/flox}$ *::Myf6*^{Cre} soleus at 2 months old. (D) KEGG functional annotations indicate carbon metabolism was affected in *Tmem65*$^{flox/flox}$ *::Myf6*^{Cre} soleus at 2 months old. (E) KEGG functional annotations show changes in *Tmem65*$^{flox/flox}$ *::Myf6*^{Cre} soleus at 10 months old. (F) Western blot analysis of soleus muscle lysates from 2 months old control *Tmem65*$^{flox/flox}$ and *Tmem65*$^{flox/flox}$ *::Myf6*^{Cre} littermates. (n=3 in each group). Coomassie Blue staining of the protein gel shows the loading control.

functional enrichment analysis of these 120 differentially expressed proteins implicated 12 affected biological processes related to metabolic functions (Fig. 8C, Suppl. Table1). KEGG functional annotations indicated affected carbon metabolism pathway at 2 months old muscle (Fig. 8D, Suppl. Table2). At 10 months old, enrichment analysis identified 593 affected biological processes (Suppl. Table3), and 25 pathways and related diseases were identified (Fig. 8E, Suppl. Table4). At 10 months old, *Tmem65*$^{flox/flox}$*::Myf6*^{Cre} mice were extremely ill and the changes in protein expression profile were assessed long after the phenotype occurred. Therefore, the involvement of so many biological processes, pathways and related diseases may reflect systemic adaptations rather than the root cause of the phenotype. In contrast, at 2 months old, the *Tmem65*$^{flox/flox}$*::Myf6*^{Cre} muscles do not yet show an overt phenotype. Thus, the protein expression profile at 2 months is expected to be more closely related to the cause of the muscle phenotypes. At 2 months old, many metabolic processes have already been affected, and carbon metabolism was identified as the most affected pathway. To validate the changes in one carbon metabolism, we assessed the protein expression of *Psat1* and *Mthfd2*, two critical one carbon metabolism enzymes located in the cytosol and mitochondrial matrix, respectively, in soleus muscles from 2 months old mice. Both PSAT1 and MTHFD2 protein expressions were upregulated in *Tmem65*$^{flox/flox}$*::Myf6*^{Cre} soleus muscles compared to soleus muscles from their littermates at 2 months old as detected by Western blot (Fig. 8F). Thus, muscle-specific loss of Tmem65 led to an up regulation of one carbon metabolism which preceded the systemic metabolic adaptations observed at 10 months of age.

Loss of TMEM65 in primary fibroblasts leads to increased uncoupling, fragmentation, and removal of mitochondria

To further investigate the role of TMEM65 at the cellular level, primary fibroblasts were cultured from lung tissues of P7 pups. Fibroblasts isolated from lung tissue of *Tmem65*$^{+V5/+V5}$ were stained with anti-V5 antibody to visualize the localization of TMEM65-V5 within the cell. Suppl Fig. 6 shows that TMEM65-V5 staining colocalized with MitoTracker Red, confirming mitochondrial localization of TMEM65 in fibroblasts. To compare mitochondrial morphology, *Tmem65*$^{+/+}$ Control and *Tmem65*$^{-/-}$ cells were loaded

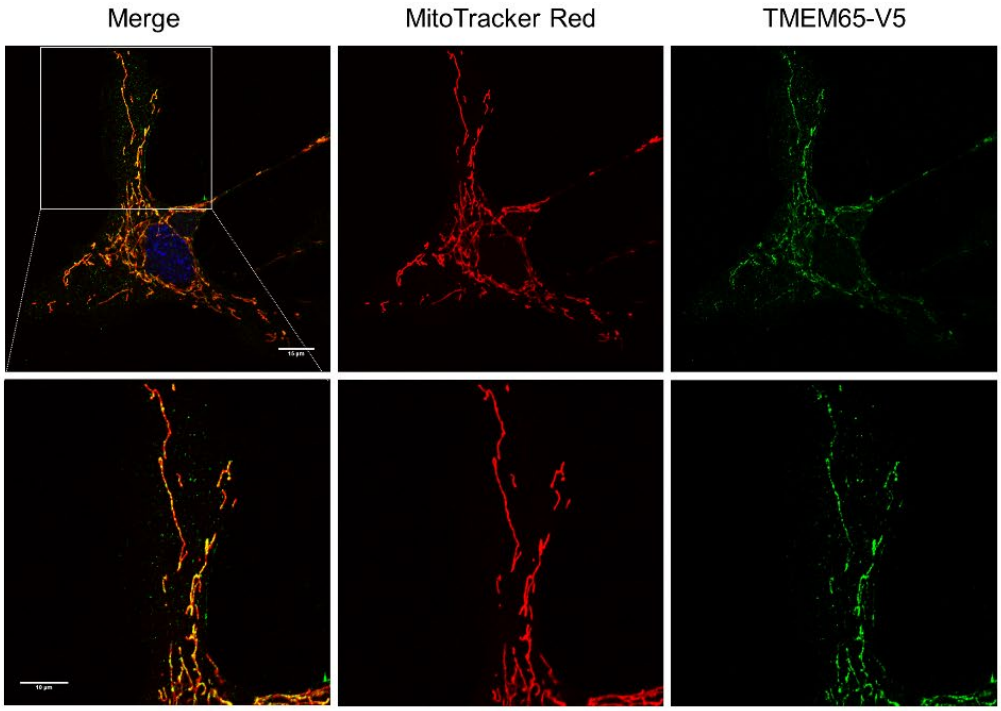

Supplemental figure 6. Colocalization of TMEM65 with MitoTracker Red in primary fibroblast. Primary fibroblast from *Tmem65*$^{V+/V+}$ pup was stained with anti-V5 antibody (green) and MitoTracker Red. Nucleus was stained with DAPI (Blue).

with MitoTracker Red to visualize the mitochondria. Mitochondria of *Tmem65*$^{-/-}$ cells were more likely to be fragmented, while mitochondria in control cells were mostly tubular (Fig. 9A and 9B), suggesting loss of TMEM65 moved the balance between mitochondrial fission and fusion to a more pro-fission state. Since mitochondrial dynamics are essential to maintenance of mitochondrial quality control (25), we next evaluated whether ablation of TMEM65 affects mitochondrial turnover. *Tmem65*$^{+/-}$ mice were crossed with the mito-QC mouse, a transgenic line with a pH-sensitive, fluorescent mitochondrial signal used to visualize mitophagy, the essential quality-control mechanism of mitochondria in the cell (26). Similar to *Tmem65*$^{-/-}$ cells, the mitochondria of *Tmem65*$^{-/-}$::mito-QC fibroblasts were more fragmented (Fig. 9C). Moreover, more mitolysosomes were observed in *Tmem65*$^{-/-}$::mito-QC fibroblasts (Fig. 9D), indicating loss of TMEM65 leads to increased rates of mitochondrial degradation and removal through mitophagy.

To evaluate the impact of TMEM65 on mitochondrial functional activity, mitochondrial membrane potentials of control and *Tmem65*$^{-/-}$ fibroblasts were measured with tetramethyl rhodamine, methyl ester (TMRM) (Fig. 9E). Using the fully reduced endogenous NADH autofluorescence signal to normalize for mitochondrial content, membrane potentials of *Tmem65*$^{-/-}$ mitochondria were significantly lower than controls, suggesting a partial collapse of the protonmotive force in *Tmem65*$^{-/-}$ mitochondria. We next measured the rate of mitochondrial energy conversion in single cells by using mitoRACE (27) to assess NADH kinetics upon rapid inhibition of NADH utilization with cyanide . *Tmem65*$^{-/-}$ fibroblasts showed altered NADH redox kinetics compared to control (Fig. 9F). *Tmem65*$^{-/-}$ fibroblasts were more oxidized at baseline (Fig. 9G) and had an ~2-fold greater basal NADH flux (Fig. 9H) compared to WT control fibroblasts. In summary, these data suggest that ablation of TMEM65 in primary fibroblasts results in partial mitochondrial uncoupling leading to fragmentation followed by mitophagy.

DISCUSSION:

In this study, we knocked out a mitochondrial protein, TMEM65, in mouse through a reverse genetics approach to help understand the function of TMEM65 protein. We showed that TMEM65 is widely expressed in different organs and tissues in mouse, including brain, heart, skeletal muscles, smooth

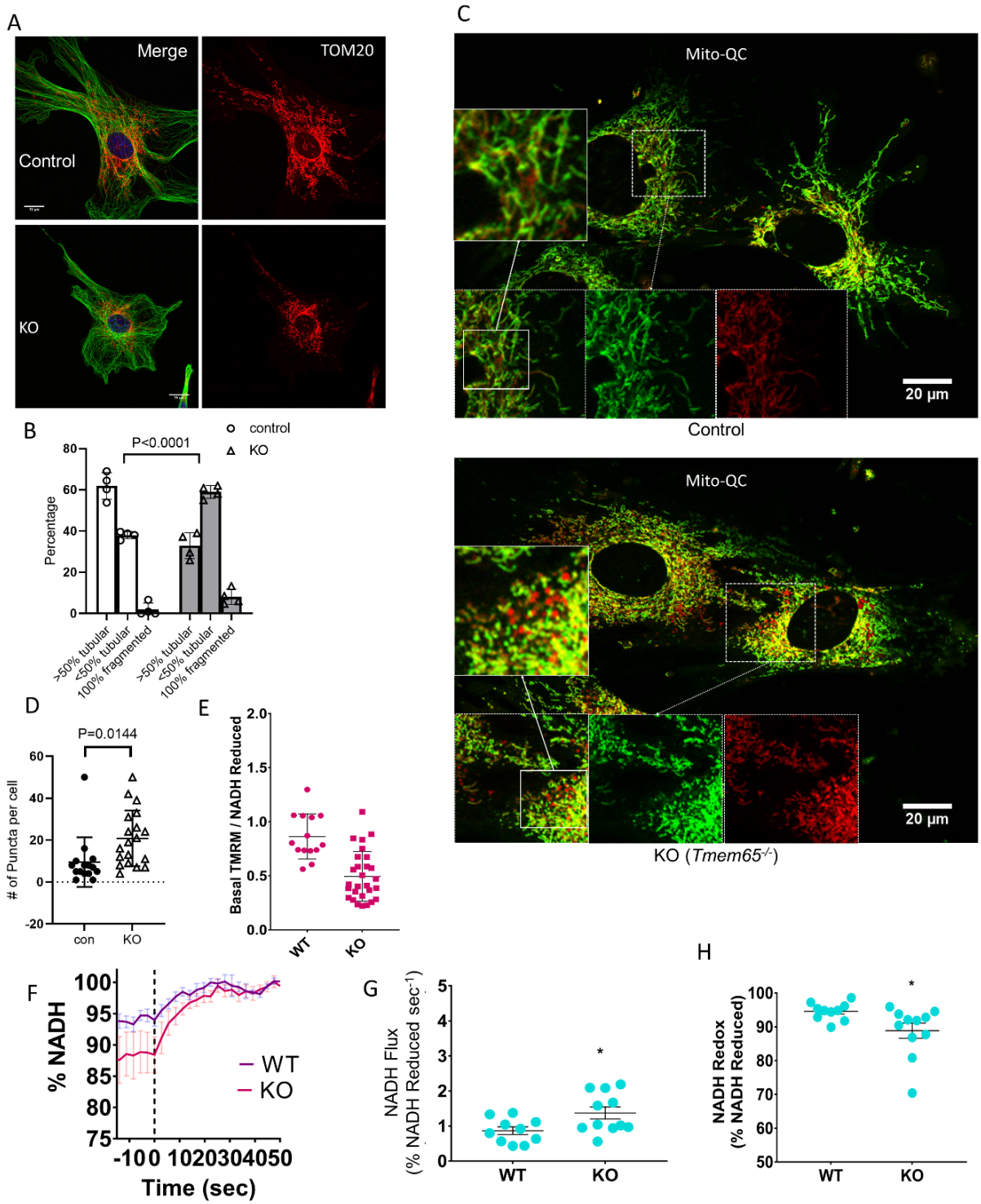

Figure 9. Loss of Tmem65 in primary fibroblasts leads to increased uncoupling, fragmentation, and removal of mitochondria. (A) Mitochondria were more fragmented in *Tmem65*$^{-/-}$ fibroblasts. Control and *Tmem65*$^{-/-}$ fibroblasts stained with anti-TOM20 (red), anti-tubulin (green) antibodies and DAPI. (B) Quantification of mitochondrial morphology. (C) *Tmem65*$^{-/-}$ ::mito-QC fibroblasts contain more fragmented mitochondria and more mitolysosomes compared to control *Tmem65*$^{+/+}$ ::mito-QC. (D) Quantification of mitolysosomes. (E) Mitochondrial membrane potentials measured with TMRM. (F) MitoRACE measurement of NADH autofluorescence kinetics during the mitochondrial redox after cyanide application shows a different NADH redox kinetics compared to control. (G) Quantification of mitochondrial flux from wild type control and *Tmem65*$^{-/-}$ fibroblasts. (H) Mitochondrial NADH redox status of wild type control and *Tmem65*$^{-/-}$ fibroblasts.

muscles, kidney, among others. We found that systemic ablation of TMEM65 in mice is fatal with *Tmem65*$^{-/-}$ mice dying at wean age of about 20 days old with epilepsy. Severe neurodegenerative pathological changes were found in the brain tissue. Growth retardation, weakness, occasional pulling/paralysis of hindlimb, and uncoordinated walking were also observed in these mice, which are typical symptoms of mitochondrial encephalomyopathy(17, 28). Nervous system specific KO of *Tmem65* also led to lethal epilepsy at about 20 days of age, confirming that mitochondrial encephalopathy and neurodegeneration is the major cause of death in *Tmem65* KO mice.

We then systematically knocked out *Tmem65* in striated muscle tissues which are involved in mitochondrial disorders to further identify the phenotypes. Mice of heart specific KO of *Tmem65* (*Tmem65*$^{flox/flox}$ *::Nkx2-5*^{Cre}) are overall healthy and capable of breeding with no baseline phenotypes. Their heart structure and function are normal though mitochondrial cytochrome levels and respiratory complexes were slightly lower in adult *Tmem65*$^{flox/flox}$ *::Nkx2-5*^{Cre} hearts. Reduced heart rate was found in one year old *Tmem65*$^{flox/flox}$ *::Nkx2-5*^{Cre} mice in the high dose Dobutamine challenge tests, and among these, only a few showed arrhythmia. Our results do not support TMEM65 as an intercalated disc protein in the heart (10). Specifically, we ruled out the localization of TMEM65 in intercalated disc with anti-TMEM65 antibody staining in WT and *Tmem65*$^{-/-}$ hearts, or anti-V5 tag antibody with the TMEM65 in-frame V5 KI (*Tmem65*$^{+V5/+V5}$) hearts. On the contrary, we found a typical mitochondrial localization patterns using these two antibodies in either isolated myocytes or frozen sections of heart tissues. Therefore, the cardiac manifestations in high dose Dobutamine test are likely related to the mitochondrial defects in the heart of *Tmem65* KO mice.

In contrast, ablation of TMEM65 specific to skeletal muscle resulted to severe mitochondrial myopathy. Skeletal muscle specific *Tmem65* KO mice (*Tmem65*$^{flox/flox}$*::Myf6*^{cre}) failed to gain weight and started to lose weight at around 3 months old, accompanied with loss of skeletal muscle mass. In muscle histochemistry, CSA of single *Tmem65* KO muscle fibers was progressively reduced, suggesting a muscular atrophy phenotype which could contribute to the observed reduction in running performance

and endurance. Furthermore, a greater reduction of type IIa muscle fibers was observed in soleus muscle compared to type I muscle fibers which caused a change in the ratio of type I and type IIa muscle fibers. Consistently, TMEM65 was previously shown to be highly expressed in type IIa fibers compared to type I fibers by high-throughput proteomics of single skeletal muscle fibers (24). Therefore, loss of TMEM65 would be expected have a stronger impact in type IIa fibers than in type I fibers. In metabolic monitoring experiments, *Tmem65*$^{flox/flox}$*::Myf6*^{Cre} mice showed higher daily feeding, energy expenditure and respiratory exchange ratio compared to littermate controls, despite similar daily mobility. In voluntary wheel running tests, *Tmem65*$^{flox/flox}$*::Myf6*^{Cre} mice had a significantly lower running distance throughout the testing period. The increase in metabolic rate not relative to activity levels is indicative of a decreased metabolic efficiency in *Tmem65* KO mice suggesting a mitochondrial uncoupling phenotype. Indeed, in the *in vitro* primary fibroblast cultures, we found that ablation of TMEM65 reduced mitochondrial membrane potential and NADH redox state while increasing basal energetic flux which is also consistent with mitochondrial uncoupling (27). Moreover, the shift in mitochondrial fusion/fission dynamics towards a more pro-fission state leading to more fragmented mitochondria as well as the greater rate of mitophagy are all consistent with a mitochondrial uncoupling phenotype (29). Interestingly, previous work in HepG2 cells showed that depletion of TMEM65 led to decreased mitochondrial membrane potential and an increase in mRNA levels of enzymes involved in redox signaling suggesting apoptosis was mildly induced due to TMEM65 depletion (30). These observations are consistent with our primary *Tmem65*$^{-/-}$ fibroblast culture results. Therefore, our data suggest that TMEM65 protein is critical for maintaining normal mitochondrial function and dynamics at the cellular level. Additionally, the mitochondrial fragmentation in *Tmem65* KO cells may also reflect a consequence of mitochondrial dysfunction and pathogenic processes. Altered mitochondrial dynamics has also been implicated in neurodegeneration (31), which was the major cause of lethality in *Tmem65*$^{-/-}$ mice.

Our mouse model showed that ablation of TMEM65 causes fatal mitochondrial encephalomyophathy which faithfully mimics the phenotypes of a patient recently reported to have decreased TMEM65

expression level as a result of a homozygous mutation at splice site of *TMEM65* gene (1). Similar to our mouse model, the patient had severe neurological symptoms including microcephaly, onset of seizures and developmental regression, without showing evidence of cardiomyopathy by echocardiography. The similarity between our *Tmem65* KO mouse model and this patient further suggests that loss of TMEM65 is the central cause of the progressive neurodegeneration in the patient. In our mouse model, we found that one carbon metabolism is affected in skeletal muscle prior to manifestation of any major phenotypes. One carbon metabolism is critical for nervous system development and neural programming (32). Crucial reactions of one carbon metabolism inside the mitochondria are catalyzed by members of the methylenetetrahydrofolate dehydrogenase (MTHFD) family. MTHFD2 is generally only expressed in transformed cells and embryonic or nondifferentiated tissues, but not in adult, differentiated tissues (33), and *Mthfd2* null mice are embryonically lethal (34). The up-regulated MTHFD2 protein level in adult skeletal muscle tissues of muscle specific *Tmem65* KO mice strongly indicate compensation for increased mitochondrial one-carbon (1C) flux and formate production. Interestingly, ablation of MTHFD1L, another critical enzyme of one carbon metabolism within the mitochondria, is not only embryonically lethal but also leads to neural tube defects in mice (35). Thus, manipulation of one carbon metabolism could be a potential therapeutic approach to the pathology resulting from a loss of TMEM65 protein.

As mentioned above, TMEM65 expression has been shown to be regulated *in vitro* by steroid receptor RNA activator (SRA), a long non-coding RNA forming a ribonucleoprotein complex with LRPPRC and SLIRP proteins (9). Interestingly, mutations of LRPPRC are the cause of Leigh syndrome French-Canadian type (LSFC) (36). As a downstream gene under the regulation of SRA, knock down of SRA complex significantly reduced TMEM65 expression level *in vitro* (9). Since *Tmem65* KO mice display a severe neurological disorder similar to LSFC, the disruption of TMEM65 expression could partially contribute to LSFC syndromes.

In summary, we demonstrate here that our *Tmem65* KO mouse model is beneficial for understanding the physiological significance of this protein and the resultant mitochondrial encephalomyopathy, and may

aid in the development of therapeutics. TMEM65 is widely expressed in different tissues, including brain, heart, skeletal muscle, smooth muscle, kidney, but not in the liver. As all these tissues and organs need mitochondria for energy conversion and biosynthesis, it will be important to further unravel the tissue specific functions and regulation of mitochondria by TMEM65.

Methods

Generation of transgenic mice

All mouse procedures were performed in accordance with institutional guidelines for animal studies and were approved by the National Heart, Lung, and Blood Institute Animal Care and Use Committee. To investigate the in vivo function of *Tmem65* gene, we first attempted to generate a mouse line with total body *Tmem65* knockout by co-microinjecting Cas9 mRNA with two single guide RNAs (sgRNAs) targeting Exon 1(Tmem-Ex1: GCCGTGTTCAGCGCCTCCAT*GGG*; the italic and underlined nucleotides are PAM) and Exon 4 (Tmem-Ex4: GCGATACCTTTCGTAGGGTT*TGG*) into zygotes collected from C57BL/6N mice, but all of the 19 offspring died between 2- and 4-week of age. Since hybrid mice show hybrid vigor and sometimes can help overcoming lethality, we next injected the same CRISPR reagents into zygotes collected B6CBA/F1 hybrid mice (JAX #100011), but again all of the 26 offspring died between 2 and 4 weeks. Some of these offspring were genotyped by PCR either shortly before or shortly after their death, and all of them turned out to be homozygous mutants, indicating that these pair of sgRNAs are extremely potent at making deletions at their target sites. In attempting to obtain heterozygous mutant mice by reducing CRISPR cutting potency, we then microinjected Cas9 mRNA with each of these two sgRNAs alone. All of the 18 offspring injected with Tmem-Ex4 sgRNA died, and all but one of the 24 pups injected with Tmem-Ex1 sgRNA died before they are one month old. The single surviving mouse appeared normal and bred well, PCR and sequencing analyses of this founder and its offspring revealed that this line had a 3bp deletion in Exon 1, which led to the in frame deletion of E58 from the TMEM65 protein. Therefore, it is a point mutation mouse line rather than a *Tmeme65* knockout .

The *Tmem65* conditional KO mouse line was generated by sequentially inserting loxP sites into Intron 3 and Intron 4, so that Exon4 can be excised by exposing to cre recombinase. Exon 4 excision can lead to translation frame shift, while Exon 2 and Exon 3 excision can only lead to in frame deletion of 27 amino acids and 15 amino acids, respectively. Briefly, the Intron 3 loxP was inserted by co-microinjecting Cas9 mRNA with the Tmem-In3 sgRNA (GTAGTTTTGTGATAGTCCTC*AGG*) and the Tmem-In3 donor oligos (GAATGTAGGCATTTTTAAAAATTATTATTACAAATACAGAGATTAGTAGTTTTG TGATAGTATAACTTCGTATAGCATACATTATACGAAGTTATGGATCC CCTCAGGCACAAGA GAGAAATAGACTGGCATGTGTCAGGTTAAATGGGGGCATCCCGTG) into zygotes collected from C57BL6/N mice. The Intron 4 loxP was inserted by co-microinjecting Cas9 mRNA with the Tmem-In4 sgRNA (CATTCTAGAAGTACAGCTAG*AGG*) and the Tmem-In4 donor oligos (TCACGTTGCAACATCTTCTGCCTTCGTTGTGTTGTGTAGTATTATGAAAAGTTCCCTCTAGAT AACTTCGTATAGCATACATTATACGAAGTTATAAGCTTCTGTACTTCTAGAATGCTTTATGGA TTCAACTATTTTGGATATTAGCAGTAAATAGACTG) into zygotes collected from mice that already contain the Intron 3 loxP site. Mice containing both loxP sites on the same allele were expanded and use for conditional knockout experiments.

The TMEM65-V5 mouse line was generated by adding a V5 tag sequence in-frame to the c-terminus of the Tmem65 gene, immediately before the stop codon. Briefly, Cas9 mRNA was co-microinjected with the Tmem-V5 sgRNA (ATCTTCTTATAGGTGTTCTA*AGG*) and the Tmem-V5 donor oligos (GGAATGTTCCCGTTGATTTTCTTTGGAGGAAGTGAAGAGGATGAGAAACTGGAAACAACAA ATGGCAAGCCCATCCCCAACCCCCTGCTGGGCCTGGACAGCACCTAATCACGTTTCAACACC TATAAGAAGATGTAAACTAATGTACCTCATCATTAACTATACTGTCCCCACAGTTAGC) into zygotes collected from the Tmem65 conditional knockout mice. Mice containing both an intact V5 tag and correctly floxed Exon 4 were bred and used for experiments.

Mouse line genotyping

Genomic DNA was extracted from mouse tail snips and standard PCR was performed for genotyping.

Primer used for genotyping:

5' floxed site:

Forward: aaggactgcacagagatgtc

Reverse: acttgacaggagttatgctg

3' floxed site:

Forward: cattctagactaccttaggtg

Reverse: gttagactctgtgaagctcac

Western Blot analysis

Mouse tissues were harvested and lysed mechanically with homogenizer in 1x RIPA lysis buffer (20-188, Sigma-Aldrich) containing 1x proteinase inhibitor cocktail (P8340, Sigma-Aldrich). Tissue lysates were incubated on ice for 10 minutes, and clarified by centrifugation at 10,000 x g for 10 minutes at 4 ℃ to pellet the tissue debris. Supernatants containing equal amounts of soluble proteins were mixed with 2x SDS protein sample buffer containing 100mM DTT (Sigma-Aldrich), denatured by incubating on a heat block at 98 ℃ for 5 minutes, and were loaded on NuPAGE 10% Bis-Tris protein gels (Life Technologies). The gel was running at 150 V for about one hour to separate the proteins. Proteins were then transferred from Bis-Tris gel onto PVDF membrane via XCell II blot module (Invitrogen) for immunoblotting. The PVDF membrane blots were blocked with blocking buffer (Li-Cor P/N927-40000) for one hour, incubated in blocking buffer containing 0.1% Tween and primary antibodies for 3 hours at room temperature or overnight at 4 ℃, washed 3 times with 1x PBS containing 0.1% Tween (PBST), incubated with blocking buffer containing 0.1% Tween and IRDye secondary antibodies (Li-Cor), washed 3 times with PBST, and imaged with Azure c600 imaging system (Azure Biosystems). Chameleon duo pre-stained protein ladder (Li-Cor 928-60000) was used as a reference of molecular weights for detected

proteins. The primary antibodies used were anti- TMEM65 (HPA025020, Sigma-Aldrich, 1:400), V5 (R960-25, Life Technologies, 1:2K), V5 (13202S, Cell Signal Technology, 1:1K), α-tubulin (P/N 926-42212, Li-Cor, 1:2K), PSAT1 (PA5-22124, Invitrogen, 1:1K), MTHFD2 (PA5-28169, Invitrogen, 1:1K). Other anti-TMEM65 antibodies tested were ab179390 (Abcam, 1:500), ab107871 (Abcam, 1:500), ab236861 (Abcam, 1:500), sc-398520 (Santa Cruz, discontinued, 1:1K). These anti-TMEM65 antibodies fail to detect specific TMEM65 protein in immunoblotting analysis.

Tissue harvesting and fixation for H&E staining

Under anesthesia, P20 or older mice were perfused with 1xPBS solution, followed by perfusion of 1xPBS containing 4% paraformaldehyde (PFA). Mouse Brain tissue was dissected out and fixed in 1xPBS containing 4% PFA at 4 ºC overnight. The fixed brain tissue was washed with 1xPBS, and stored in 70% ethanol for paraffin embedding.

Confocal microscopy

Mouse was anesthetized with 5% Isoflurane through gas anesthesia system, and was perfused through heart with 1xPBS and then 4% paraformaldehyde in 1xPBS. Mouse tissue was harvested and further fixed for 4 hours. Fixed tissue was washed with 1x PBS, and transferred into 30% sucrose in 1xPBS solution overnight till tissue sank to the bottom of the solution. The tissue was trimmed and embedded in optimal cutting temperature (O.C.T.) compound (Sakura). 10 µm sections were cut in cryostat at -20℃. Frozen tissue sections were blocked with blocking buffer (1xPBS containing 5% goat serum and 1% bovine serum albumin) for one hour, and then incubated in blocking buffer containing 0.05% Tween and primary antibodies overnight. Sections were washed 3 times with PBS containing 0.05% Tween, and then incubated in Alexa Fluor secondary antibodies (Invitrogen) for one hour. Coverslips were mounted on the sections with coverslips with Prolong gold antifade mountant (Life Technologies) after 3 washes of 1xPBS containing 0.05% Tween. Confocal images were collected with a Zeiss LSM 780 confocal microscope system. Primary antibodies used were to ATP5A (ab14748, Abcam, 1:200), V5 (13202S, Cell

Signal Technology, 1:100; or R960-25, Life technologies, 1:200), TMEM65 (HPA025020, Sigma-Aldrich, 1:50), Desmin (D1033, Sigma-Aldrich, 1:100), Connexin 43 (ab11370, Abcam, 1:400), Myosin heavy chain type I (BA-D5, DSHB, 1:60), Myosin heavy chain type IIa (SC-71, DSHB, 1:100), Myosin heavy chain type IIb (BF-F3, DSHB, 1:80), Laminin (L9393, Sigma-Aldrich, 1:200).

Inverted grip suspension test

7 wild type (WT) and 6 KO mice of P21 were subject to inverted grip strength tests. Mouse was gently placed on top of a wire grid to allow its paws to attach the grid with its torsi horizontal. The grip was gently inverted 180 degrees so the mouse was suspended above a padded surface. Latency to fall was record and averaged for three trials, separated by a rest period. The maximum trial length was set to 180 seconds.

Home cage monitoring

Paired breeding mice with new born liters containing at least 1 WT and 1 KO pups were moved into PhenoTyper home cages (Noldus, Wageningen, Netherlands) equipped with camera mounted in the cage lids for 24 hour video monitoring to record episodes of epilepsy and any other behavior changes in the pups.

Indirect calorimetry

The Oxymax-CLAMS setup (Columbus Instruments) was used to assess mouse metabolism. Mice were singly housed in the CLAMS chambers, received food and water *ad libitum* throughout the experiment, and were checked on at least twice a day throughout the experiment. Oxygen consumption, carbon dioxide production, food intake, and beam breaks (locomotion) were monitored during the experiment. The resulting data was analyzed using CalR.

Body composition

Whole body lean and fat mass was measured using the EchoMRI™ body composition analyzers for live mice.

Magnetic resonance imaging (MRI)

A total of thirteen 20, 21, and 23 days old littermates of WT and KO pups (7 KOs and 6 WTs) were anesthetized with 5% Isoflurane through gas anesthesia system and perfused with 1xPBS, and then 1xPBS containing 4% PFA and Magnevist (1:500, Bayer HealthCare Pharmaceuticals) to enhance the brain with MR contrast. The mouse head was dissected out and the skin was removed to obtain the brain within the skull. The samples were then stored in 1xPBS containing 4% PFA in 4 ℃ refrigerator. The brain remained inside the cranium for scanning to preserve the brain anatomy. Before the scan, samples were washed and equilibrated in 1xPBS for at least 24 hours.

MRI acquisition was performed ex vivo on a 14T Bruker (Billerica, MA, USA) microimaging system with a 10mm linear radio frequency coil. A T2-weighted image was acquired using a 3D multislice multiecho (MSME) pulse sequence with 100 µm isotropic resolution and a matrix size of 160 x 84 x 80, and with TE/TR = 30/3000, nex = 1. To examine brain volume, masks for the brain parenchyma were created that excluded skull and other non-brain material using the automatic segmentation snake tool in ITK-SNAP (37). The volumes of these parenchymal brain masks were measured using ITK-SNAP and the values were plotted for each specimen.

Echocardiography and electrocardiography

Mouse heart echocardiography and electrocardiography (ECG) were performed at the NHLBI Phenotyping Core. Mice were lightly anesthetized with isoflurane and placed supine over a heated platform with ECG leads and a rectal temperature rpobe. The Vevo2100 ultrasound system (VisualSonics, Toronto, Canada) with a 30 MHz ultrasound probe (VisualSonics, MS-400 transducer) was used to acquire heart images. Measurements were made from standard 2D and M mode images from the parasternal long axis and mid-papillary short axis views of the left ventricle.

Dobutamine stress echocardiography

Mice were lightly anesthetized with isoflurane during examination and placed supine on a heated platform with ECG leads and a rectal temperature probe. Heart images were acquired using the Vevo2100 ultrasound system (VisualSonics) with a 30-MHz ultrasound probe (VisualSonics, MS-400 transducer). After a baseline scan, mice were given a constant rate infusion of dobutamine (0.625 mg/ml in normal saline containing 5% dextrose) via the tail vein using an infusion syringe pump (Harvard Apparatus). The first infusion was at the low dose of 10 μg/kg/min. After the heart rate reached a steady state as determined by the ECG, infusion rate was increased to 40 μg/kg/min, and the scans were repeated. Echocardiograph scans were collected after the low and high dose infusions. Post imaging analysis was conducted using Vevo2100 analysis software to measure %EF, %FS, and cardiac chamber dimensions from 2-D and M-mode images.

Mass spectrometry

Muscle tissue preparation and mass spectrometry was performed as previously described (38). Briefly, frozen soleus muscles were individually transferred to 130 μl of urea based lysis buffer, 6 M Urea, 2 M Thiourea, 50 mM Triethylammonium bicarbonate (TEAB). Tissues were homogenized with ceramic beads using 3 cycles of 40s at 5500 rpm and 4°C (Precellys® Cryolys Evolution, Bertin Technologies). Tissue lysates were further clarified by microcentrifuge spin columns (QIAshredder, Qiagen) to obtain clear protein lysate centrifuged at 10,000g for 2min at 4°C. The extracted protein supernatants were transferred to 1.5 ml microtubes for further processing. Bradford assay (Thermo Fisher Scientific) was used to estimate the protein concentration of lysate, 100 μg of each lysate was reduced, alkylated, delipidated, digested with trypsin and individually labeled with Tandem Mass Tag (TMT) 16plex labeling reagent kit as per manufacturer's instructions (Thermo Fisher Scientific).

High pH reversed-phase liquid chromatography was performed on an offline Agilent 1200 series HPLC. The quenched TMT labeled peptides were all combined, concentrated and desalted using HLB Oasis 1cc,

Waters) column per manufacturer's instructions. The dried desalted peptides were resuspended in 0.1 ml 10 mM triethyl ammonium bicarbonate with 2% (v/v) acetonitrile. Peptides were loaded onto an Xbridge C18 HPLC column (Waters; 2.1mm inner diameter x 100 mm, 5µm particle size), and profiled with a linear gradient of 5–35 % buffer B (90% acetonitrile, 10 mM triethyl ammonium bicarbonate) over 60 min, at a flowrate of 0.25 ml/min. The chromatographic performance was monitored by sampling the eluate with a diode array detector (1200 series HPLC, Agilent) scanning between wavelengths of 200 and 400 nm. Fractions were collected at 1min intervals followed by fraction concatenation. Twelve concatenated fractions were dried and resuspended in 0.01% formic acid, 2% acetonitrile. Approximately 500 ng of peptide mixture was loaded per liquid chromatography-mass spectrometry run.

All fractions were analyzed on an Ultimate 3000-nLC coupled to an Orbitrap Fusion Lumos Tribrid instrument (Thermo Fisher Scientific) equipped with a nanoelectrospray source. Peptides were separated on an EASY-Spray C18 column (75 µm x 50cm inner diameter, 2 µm particle size and 100 Å pore size, Thermo Fisher Scientific). Peptide fractions were placed in an autosampler and separation was achieved by 120 min gradient from 4-40% buffer B (100% ACN and 0.1% formic acid) at a flow rate of 300 nL/min. An electrospray voltage of 1.9 kV was applied to the eluent via the EASY-Spray column electrode. The Lumos was operated in positive ion data-dependent mode, using Synchronous Precursor Selection (SPS-MS3). Full scan MS1 was performed in the Orbitrap with a precursor selection range of 380–1,400 m/z at nominal resolution of 1.2 x 105. The AGC target and maximum accumulation time settings were set to 4 x 105 and 50 ms, respectively. MS2 was triggered by selecting the most intense precursor ions above an intensity threshold of 5 x 103 for collision induced dissociation (CID)-MS2 fragmentation with an AGC target and maximum accumulation time settings of 2 x 104 and 75 ms, respectively. Mass filtering was performed by the quadrupole with 0.7 m/z transmission window, followed by CID fragmentation in the linear ion trap with 35% normalized collision energy in rapid scan mode and parallelizable time option was selected. SPS was applied to co-select 10 fragment ions for HCD-MS3 analysis. SPS ions were all selected within the 350–1,300 m/z range and were set to preclude

selection of the precursor ion and TMTC ion series. The AGC target and maximum accumulation time were set to 1 x 105 and 150 ms (respectively) and parallelizable time option was selected. Co-selected precursors for SPS-MS3 underwent HCD fragmentation with 55% normalized collision energy and were analyzed in the Orbitrap with nominal resolution of 5 x 104. The number of SPS- MS3 spectra acquired between full scans was restricted to a duty cycle of 3 s.

Raw data files were processed using Proteome Discoverer (v2.4, Thermo Fisher Scientific), with Sequest HT (Thermo Fisher Scientific) search node. The data files were searched against UniProtKB/Swiss-Prot mus musculus (17,030 reviewed, release 2020_10) protein sequence database, with carbamidomethylation of cysteine, TMT-Pro (+304.207) modification of lysines and peptide N-terminus set as static modifications; oxidation of methionine as dynamic. For SPS-MS3, the precursor and fragment ion tolerances of 10 ppm and 0.5 Da were applied, respectively. Up to two-missed tryptic cleavages were permitted. Percolator algorithm (v.3.02.1, University of Washington) was used to calculate the false discovery rate (FDR) of peptide spectrum matches (PSM), set to a q-value <0.05. TMT 16-plex quantification was also performed by Proteome Discoverer by calculating the sum of centroided ions within 20 ppm window around the expected m/z for each of the 15 TMT reporter ions. Spectra with at least 60% of SPS masses matching to the identified peptide are considered as quantifiable PSMs. Quantification was performed at the MS3 level where the median of all quantifiable PSMs for each protein group was used for protein ratios. The mass spectrometry proteomics data have been deposited to the ProteomeXchange Consortium (dataset identifier PXD035605) via MassIVE (UCSD, San Diego, CA, USA) a member of the consortium (dataset identifier MSV000089991.

Primary lung fibroblast culture

Lung tissues from P7 pups were minced into ~1mm pieces and digested with Librase (Roche) in DMEM/F12 media at 37 degree for 1 hour. Digested tissues were washed with warm DMEM/F12 media containing 15% FBS and 1x antibiotic/antimycotic, then cultured at 37 ℃/5% CO2 in 10cm plates with DMEM/F12 media containing 15% FBS and 1x antibiotic/antimycotic to allow fibroblasts to crawl out of

the tissue fragments and attach to the plate. Cells were sub-cultured with 1:2 split when needed. After 2 weeks, cells were harvested and sub-cultured in a new plate with EMEM containing 10% FBS, 1xPenicillin/Streptomycin, non-essential amino acids, and sodium pyruvate.

Multiphoton laser-scanning fluorescence microscopy

Fibroblasts were loaded with 20 nM TMRM for 30 minutes before imaging. TMRM and endogenous NAD(P)H signals from mitochondria were acquired with an upright Leica SP8 multiphoton microscope with resonant scanning and a Nikon 25× (1.1 NA) water-immersion objective according to the protocol published in Willingham TB et al. (27). TMRM and NADH fluorescence were excited using a Ti:Sapphire laser tuned to 710 nm or 750 nm and emissions detected by a non-descanned Leica HyD detector in the 414–538 nm range for NADH, and 538-605 nm range for TMRM.

Statistics

Results are expressed as mean±SD. Statistical analyses were performed using GraphPad Prism 9 or SigmaPlot 14.0 software. All data were tested for normality before analysis. If the normality test passed, comparisons were performed by the 2-tailed unpaired Student's t test. If not, the nonparametric Mann-Whitney Rank Sum test was used. P value was reported on each test. A P value of less than 0.05 was considered statistically significant.

Study approval

Animal studies were approved by the National Heart, Lung, and Blood Institute Animal Care and Use Committee.

AUTHOR CONTRIBUTIONS

YZ and BG designed research studies. YZ, TBW, BG, LR, MA, CL, DS, AN, AMA, JM, and RC conducted experiments. YZ, TBW, LR, and DS analyzed data. YZ and BG wrote the manuscript.

ACKNOWLEDGEMENTS

The authors thank Ian Ganley (University of Dundee) for kindly providing the mito-QC mice and Robert Balaban and Vamsi Mootha for help with initial screens which identified *Tmem65* as a gene of interest. We thank Ms. Michele Allen of Murine Phenotyping Core for assistance in conducting experiments. We thank the NHLBI Light Microscopy Core and NHLBI Electron Microscopy Core for assistance with imaging. Support for this work was provided by the Division of Intramural Research, National Heart, Lung, and Blood Institute and the Intramural Research Program, National Institute of Arthritis and Musculoskeletal and Skin Diseases.

REFERENCES

1. Nazli A, Safdar A, Saleem A, Akhtar M, Brady LI, Schwartzentruber J, et al. A mutation in the TMEM65 gene results in mitochondrial myopathy with severe neurological manifestations. *Eur J Hum Genet.* 2017;25(6):744-51.
2. Nunnari J, and Suomalainen A. Mitochondria: in sickness and in health. *Cell.* 2012;148(6):1145-59.
3. Pfanner N, Warscheid B, and Wiedemann N. Mitochondrial proteins: from biogenesis to functional networks. *Nat Rev Mol Cell Biol.* 2019;20(5):267-84.
4. Pfanner N, and Wiedemann N. Mitochondrial protein import: two membranes, three translocases. *Curr Opin Cell Biol.* 2002;14(4):400-11.
5. Chacinska A, Koehler CM, Milenkovic D, Lithgow T, and Pfanner N. Importing mitochondrial proteins: machineries and mechanisms. *Cell.* 2009;138(4):628-44.
6. Spinelli JB, and Haigis MC. The multifaceted contributions of mitochondria to cellular metabolism. *Nat Cell Biol.* 2018;20(7):745-54.
7. Pagliarini DJ, Calvo SE, Chang B, Sheth SA, Vafai SB, Ong SE, et al. A mitochondrial protein compendium elucidates complex I disease biology. *Cell.* 2008;134(1):112-23.
8. Nishimura N, Gotoh T, Oike Y, and Yano M. TMEM65 is a mitochondrial inner-membrane protein. *PeerJ.* 2014;2:e349.
9. Foulds CE, Tsimelzon A, Long W, Le A, Tsai SY, Tsai MJ, et al. Research resource: expression profiling reveals unexpected targets and functions of the human steroid receptor RNA activator (SRA) gene. *Mol Endocrinol.* 2010;24(5):1090-105.
10. Sharma P, Abbasi C, Lazic S, Teng ACT, Wang D, Dubois N, et al. Evolutionarily conserved intercalated disc protein Tmem65 regulates cardiac conduction and connexin 43 function. *Nat Commun.* 2015;6:8391.
11. Hanke T, Szawlowski P, and Randall RE. Construction of solid matrix-antibody-antigen complexes containing simian immunodeficiency virus p27 using tag-specific monoclonal antibody and tag-linked antigen. *J Gen Virol.* 1992;73 (Pt 3):653-60.

12. Schwenk F, Baron U, and Rajewsky K. A cre-transgenic mouse strain for the ubiquitous deletion of loxP-flanked gene segments including deletion in germ cells. *Nucleic Acids Res.* 1995;23(24):5080-1.
13. Sato S. Quantitative evaluation of ontogenetic change in heart rate and its autonomic regulation in newborn mice with the use of a noninvasive piezoelectric sensor. *Am J Physiol Heart Circ Physiol.* 2008;294(4):H1708-15.
14. Moses KA, DeMayo F, Braun RM, Reecy JL, and Schwartz RJ. Embryonic expression of an Nkx2-5/Cre gene using ROSA26 reporter mice. *Genesis.* 2001;31(4):176-80.
15. Balaban RS, Mootha VK, and Arai A. Spectroscopic determination of cytochrome c oxidase content in tissues containing myoglobin or hemoglobin. *Anal Biochem.* 1996;237(2):274-8.
16. Burte F, Carelli V, Chinnery PF, and Yu-Wai-Man P. Disturbed mitochondrial dynamics and neurodegenerative disorders. *Nat Rev Neurol.* 2015;11(1):11-24.
17. Lake NJ, Bird MJ, Isohanni P, and Paetau A. Leigh syndrome: neuropathology and pathogenesis. *J Neuropathol Exp Neurol.* 2015;74(6):482-92.
18. Tronche F, Kellendonk C, Kretz O, Gass P, Anlag K, Orban PC, et al. Disruption of the glucocorticoid receptor gene in the nervous system results in reduced anxiety. *Nat Genet.* 1999;23(1):99-103.
19. Liang H, Hippenmeyer S, and Ghashghaei HT. A Nestin-cre transgenic mouse is insufficient for recombination in early embryonic neural progenitors. *Biol Open.* 2012;1(12):1200-3.
20. Hood DA, Memme JM, Oliveira AN, and Triolo M. Maintenance of Skeletal Muscle Mitochondria in Health, Exercise, and Aging. *Annu Rev Physiol.* 2019;81:19-41.
21. Keller C, Arenkiel BR, Coffin CM, El-Bardeesy N, DePinho RA, and Capecchi MR. Alveolar rhabdomyosarcomas in conditional Pax3:Fkhr mice: cooperativity of Ink4a/ARF and Trp53 loss of function. *Genes Dev.* 2004;18(21):2614-26.
22. Sambasivan R, Comai G, Le Roux I, Gomes D, Konge J, Dumas G, et al. Embryonic founders of adult muscle stem cells are primed by the determination gene Mrf4. *Dev Biol.* 2013;381(1):241-55.
23. Southard S, Low S, Li L, Rozo M, Harvey T, Fan CM, et al. A series of Cre-ER(T2) drivers for manipulation of the skeletal muscle lineage. *Genesis.* 2014;52(8):759-70.
24. Kallabis S, Abraham L, Muller S, Dzialas V, Turk C, Wiederstein JL, et al. High-throughput proteomics fiber typing (ProFiT) for comprehensive characterization of single skeletal muscle fibers. *Skelet Muscle.* 2020;10(1):7.
25. Ni HM, Williams JA, and Ding WX. Mitochondrial dynamics and mitochondrial quality control. *Redox Biol.* 2015;4:6-13.
26. McWilliams TG, Prescott AR, Allen GF, Tamjar J, Munson MJ, Thomson C, et al. mito-QC illuminates mitophagy and mitochondrial architecture in vivo. *J Cell Biol.* 2016;214(3):333-45.
27. Willingham TB, Zhang Y, Andreoni A, Knutson JR, Lee DY, and Glancy B. MitoRACE: evaluating mitochondrial function in vivo and in single cells with subcellular resolution using multiphoton NADH autofluorescence. *J Physiol.* 2019;597(22):5411-28.
28. Lake NJ, Compton AG, Rahman S, and Thorburn DR. Leigh syndrome: One disorder, more than 75 monogenic causes. *Ann Neurol.* 2016;79(2):190-203.
29. Demine S, Renard P, and Arnould T. Mitochondrial Uncoupling: A Key Controller of Biological Processes in Physiology and Diseases. *Cells.* 2019;8(8).
30. Urushima Y, Haraguchi M, and Yano M. Depletion of TMEM65 leads to oxidative stress, apoptosis, induction of mitochondrial unfolded protein response, and upregulation of mitochondrial protein import receptor TOMM22. *Biochem Biophys Rep.* 2020;24:100870.

31. Yang D, Ying J, Wang X, Zhao T, Yoon S, Fang Y, et al. Mitochondrial Dynamics: A Key Role in Neurodegeneration and a Potential Target for Neurodegenerative Disease. *Front Neurosci.* 2021;15:654785.
32. Ducker GS, and Rabinowitz JD. One-Carbon Metabolism in Health and Disease. *Cell Metab.* 2017;25(1):27-42.
33. Christensen KE, and Mackenzie RE. Mitochondrial methylenetetrahydrofolate dehydrogenase, methenyltetrahydrofolate cyclohydrolase, and formyltetrahydrofolate synthetases. *Vitam Horm.* 2008;79:393-410.
34. Di Pietro E, Sirois J, Tremblay ML, and MacKenzie RE. Mitochondrial NAD-dependent methylenetetrahydrofolate dehydrogenase-methenyltetrahydrofolate cyclohydrolase is essential for embryonic development. *Mol Cell Biol.* 2002;22(12):4158-66.
35. Momb J, Lewandowski JP, Bryant JD, Fitch R, Surman DR, Vokes SA, et al. Deletion of Mthfd1l causes embryonic lethality and neural tube and craniofacial defects in mice. *Proc Natl Acad Sci U S A.* 2013;110(2):549-54.
36. Mootha VK, Lepage P, Miller K, Bunkenborg J, Reich M, Hjerrild M, et al. Identification of a gene causing human cytochrome c oxidase deficiency by integrative genomics. *Proc Natl Acad Sci U S A.* 2003;100(2):605-10.
37. Yushkevich PA, Piven J, Hazlett HC, Smith RG, Ho S, Gee JC, et al. User-guided 3D active contour segmentation of anatomical structures: significantly improved efficiency and reliability. *Neuroimage.* 2006;31(3):1116-28.
38. Kim Y, Yang DS, Katti P, and Glancy B. Protein composition of the muscle mitochondrial reticulum during postnatal development. *J Physiol.* 2019;597(10):2707-27.